

3-4-2004

Microstructural and Superconducting Properties of V Doped MgB_2 Bulk and Wires

Oscar Eduardo Castillo
Florida State University

Follow this and additional works at: <http://diginole.lib.fsu.edu/etd>

Recommended Citation

Castillo, Oscar Eduardo, "Microstructural and Superconducting Properties of V Doped MgB_2 Bulk and Wires" (2004). *Electronic Theses, Treatises and Dissertations*. Paper 4048.

This Thesis - Open Access is brought to you for free and open access by the The Graduate School at DigiNole Commons. It has been accepted for inclusion in Electronic Theses, Treatises and Dissertations by an authorized administrator of DigiNole Commons. For more information, please contact lib-ir@fsu.edu.

THE FLORIDA STATE UNIVERSITY
COLLEGE OF ENGINEERING

MICROSTRUCTURAL AND SUPERCONDUCTING
PROPERTIES OF V DOPED MgB_2 BULK AND WIRES

By

OSCAR EDUARDO CASTILLO

A Thesis submitted to the
Department of Mechanical Engineering
in partial fulfillment of the
requirements for the degree of
Master of Science

Degree Awarded:
Spring Semester, 2004

The members of the Committee approve the thesis of Oscar E. Castillo defended on March 4, 2004.

Justin Schwartz
Professor Directing Thesis

Peter Kalu
Committee Member

Simone Peterson Hruda
Committee Member

Approved:

Chiang Shih, Chair, Mechanical Engineering

Ching-Jen Chen, Dean, College of Engineering

The Office of Graduate Studies has verified and approved the above named committee members.

TABLE OF CONTENTS

LIST OF FIGURES	v
ABSTRACT.....	vii
1. INTRODUCTION.....	1
1.1. Motivation.....	1
1.2. Superconductivity	2
1.3. Superconducting Materials	5
1.4. Scope and Objectives.....	9
2. SAMPLE PREPARATION AND CHARACTERIZATION TECHNIQUES ...	12
2.1. Sample Preparation.....	12
2.1.1. Powder Preparation	
2.1.2. Bulk Samples	
2.1.3. Groove rolled wires	
2.1.4. Drawn Wires	
2.2. Heat Treatments.....	15
2.2.1. Bulk Samples	
2.2.2. Groove rolled wires	
2.2.3. Drawn wires	
2.3. X-ray Diffraction (XRD)	17
2.4. Environmental Scanning Electron Microscope (ESEM) and Energy Dispersive Spectroscopy (EDS)	18
2.5. Superconducting Quantum Interference Device (SQUID).....	19
2.6. Transport Measurements	20

3. INVESTIGATION OF BULK SAMPLES	22
3.1. Initial Results	22
3.2. Results.....	25
3.2.1. Phase purity by XRD	
3.2.2. Superconducting Properties	
3.3. Conclusions.....	31
4. INVESTIGATION OF GROOVE ROLLED WIRE	33
4.1. Results.....	33
4.1.1. Sheath / Core interface	
4.1.2. Transport Measurements	
4.2. Conclusions.....	35
5. INVESTIGATION OF DRAWN WIRES	36
5.1. Results.....	36
5.1.1. Sheath / Core interface	
5.1.2. Microstructure and Dopant Distribution	
5.1.3. Transport Measurements	
5.2. Conclusions.....	41
6. SUMMARY AND SUGGESTIONS FOR FUTURE WORK.....	44
REFERENCES.....	46
BIOGRAPHICAL SKETCH	48

LIST OF FIGURES

Figure 1.1	An example of a superconductor's Critical Surface	2
Figure 1.2	Comparing the different reactions to an applied magnetic field between Type I and Type II superconductors.....	3
Figure 1.3	Type II superconductor in its mixed state, showing the presence of normal regions and flux lines	4
Figure 1.4	The orthorhombic perovskite crystal structure of Bi-2223, focusing on its 3 CuO ₂ planes [7]	6
Figure 1.5	The hexagonal (AlB ₂) crystal structure of MgB ₂ [7]	7
Figure 1.6	J _c dependence on magnetic field at 25 K for various forms of MgB ₂ [18].....	9
Figure 1.7	Hysteresis loop widths comparing V doped and undoped bulk samples [29].....	10
Figure 2.1	Example of unreacted Mg-V-B bulk samples	13
Figure 2.2	IRM Stanat groove rolling mill used to fabricate Mg-V-B wires	13
Figure 2.3	Relationship between time and temperature in the relief of residual stresses in steel	14
Figure 2.4	Drawing bench used to fabricate Mg-V-B wires	15
Figure 2.5	Schematic of the furnace system used	16
Figure 2.6	Schematic of XRD system	17
Figure 2.7	Superconducting ring with two Josephson Junctions.....	20
Figure 2.8	Schematic of 4-point method used to measure I _c	19
Figure 3.1	Examples of problems encountered during bulk sample fabrication	22
Figure 3.2	XRD patterns taken from Bulk sample and Alfa Aesar, prereacted MgB ₂ powder	23
Figure 3.3	XRD patterns comparing the Gray layer found on the surface of pellets with an MgB ₂ and Mg _{2.99} Ni _{7.52} B ₆ reference	24
Figure 3.4	XRD patterns of undoped (0 at%) bulk samples, reacted for 2 hours, at various temperatures.....	26
Figure 3.5	XRD patterns of undoped (0 at%) bulk samples, reacted for 1 hour, at various temperatures	27

Figure 3.6	XRD patterns of bulk samples reacted at 800 °C for 1 hour, with increasing V dopant.....	27
Figure 3.7	XRD patterns of undoped (0 at%) bulk samples, reacted at 800 °C for various reaction times	28
Figure 3.8	XRD patterns of bulk samples reacted at 800 °C for 0.3 hour, with increasing V dopant.....	28
Figure 3.9	Magnetization versus Temperature for 10 at% V doped bulk sample showing a T_c onset of 37 K.....	29
Figure 3.10	Magnetization hysteresis width of bulk samples reacted at 800 °C for 1hour, with increasing V dopant.....	30
Figure 3.11	Magnetization hysteresis width of 10 at% V doped, bulk sample reacted at 800 °C for various reaction times.....	30
Figure 3.12	Magnetization hysteresis width of 10 at% V doped, bulk sample reacted at 850 °C for various reaction times.....	31
Figure 4.1	Axial cross section of groove rolled wire having ~ 2.5 x 2.5 mm ² outer dimensions	33
Figure 4.2	Maximum I_c values measured for varying dopant concentrations in groove rolled wires	34
Figure 5.1	Axial cross section of a cold drawn wire, having an outer diameter of 1.215 mm.....	36
Figure 5.2	Longitudinal cross sections of cold drawn wire, with varying V dopant concentrations (a) $x = 0.0$, (b) $x = 0.05$, (c) $x = 0.1$, (d) $x = 0.15$	37
Figure 5.3	Micrograph taken from the core of a 5 at% doped wire, where secondary phases have been labeled	38
Figure 5.4	EDS spectra of phases in Figure 5.4	38
Figure 5.5	V vs. I plot showing the differences encountered when measuring I_c in drawn wires.....	40
Figure 5.6	Maximum I_c values measured for varying dopant concentrations and heat treatments in drawn wires.....	40
Figure 5.7	Variation of I_c values for 10 at% doped wires	41
Figure 5.8	Percentage of non-superconducting material present in 15 at% V doped wires if V is not entering the MgB ₂ phase.....	43

ABSTRACT

Studies of the effects of doping MgB_2 bulk and steel-sheathed wires with V are presented. Samples having the nominal composition $\text{Mg}_{1-x}\text{V}_x\text{B}_2$ ($x = 0, 0.05, 0.10, 0.15$) have been fabricated and investigated to understand the role of V doping on the phase formation, microstructure and superconducting properties. Characterization of superconducting samples was carried out using XRD, SQUID, ESEM/EDS, and I_c measurements. Results show an enhancement of superconducting properties with V doping, and suggest the presence of V in the superconducting phase. Wires with J_c values as high as $1.4 \times 10^5 \text{ A/cm}^2$ have been achieved.

CHAPTER 1

INTRODUCTION

1.1 Motivation

Since the discovery of superconductivity in 1911 [1], scientists and engineers have been searching for practical applications that could benefit from the unique properties of superconductors. While in the superconducting state, these materials have the ability to transport large DC currents with no measurable resistive losses. To do this, a superconductor must be kept below three critical parameters, critical temperature (T_c), critical field (H_c), and critical current density (J_c).

Loss-free current flow allows superconducting wires with relatively small cross sections to transport currents at high current densities. It is envisioned that superconductors could be used to develop electrical devices that were smaller, lighter, and more energy efficient. Although some progress has been made, limitations of the materials have prevented wide-scale use of the technology.

Before the mid-80's, superconductors were metals, and had to be operated at low temperatures, close to the boiling point of He (4.2 K). Due to the costs associated with maintaining such low temperatures, applications were limited to specialty areas such as research laboratories (particle accelerators, high field magnets, SQUIDs) and the medical industry (MRI). These applications succeeded because there were no alternative materials that could compete with the superconductors. This is not the case, however, in power applications, where Cu is the standard. Although energy and space can be saved using superconductors, it does not outweigh the costs of cooling the material or the initial costs and risks of introducing new technology.

Prospects for developing power applications rose with the discovery of high temperature superconductor (HTS) materials in the mid-80's [2,3,4]. With critical temperatures higher than the boiling point of N_2 (77 K), researchers hoped that this less expensive cryogen could be used for cooling. Unfortunately, like all superconductors, the current density in HTS materials decreases dramatically with increasing temperature. In addition, to achieve high current densities in HTS materials, either a complicated processing route (YBCO) [5] or an expensive sheath material (BSCCO) [6] is needed.

Attention is now being directed towards the recently discovered MgB_2 , which has a critical temperature of 39 K [9]. Unlike HTS materials, MgB_2 is simple and inexpensive to fabricate. Also, its T_c is at least 15 K higher than any low temperature superconductor (LTS). Currently, the largest obstacle MgB_2 faces is its poor J_c characteristics in an applied magnetic field. If the in-field properties can be improved, MgB_2 can be used for low field applications at higher temperatures than LTS materials are capable of, and for less cost than HTS materials would allow.

1.2 Superconductivity

H.K. Onnes discovered superconductivity in 1911 while investigating the electrical properties of Hg at low temperatures [1]. He found that Hg loses its electrical resistance as temperature is decreased below a critical value (T_c). Since then, superconductivity has been revealed in many other metals as well as alloys and intermetallic compounds. Later it was found that in addition to a critical temperature, both current density and applied magnetic field have to be kept below their respective critical values (J_c and H_c) to maintain the superconducting state. Figure 1.1 illustrates the superconducting state as a region beneath a shaded “critical surface”, defined by the three critical parameters, J_c , H_c , and T_c .

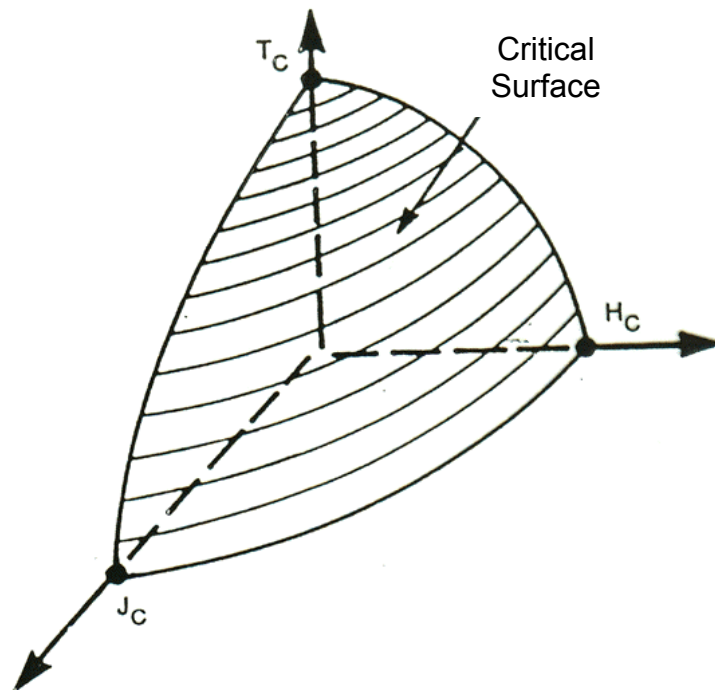


FIGURE 1.1 An illustration of a superconducting critical surface

Superconductors can be classified into two groups, based on their reaction to applied magnetic field. All superconductors behave as a perfect diamagnet, expelling all applied magnetic flux, up to a material specific limit. This phenomenon is known as the Meissner effect. Once this field is reached, Type I superconductors abruptly transition to the normal state and magnetic field fully penetrates the specimen. This usually occurs at relatively low fields ($< 85 \text{ mT}$). Type II superconductors, on the other hand, do not completely succumb to the effects of increasing magnetic field. Instead, once a critical field is reached (H_{c1}) the superconductor will begin to gradually allow magnetic flux lines to penetrate, which is known as the “mixed state”. This continues until a second critical field (H_{c2}) is reached and the penetrating flux lines completely take over the sample’s interior. The differences between the two superconductor types are illustrated in figure 1.2.

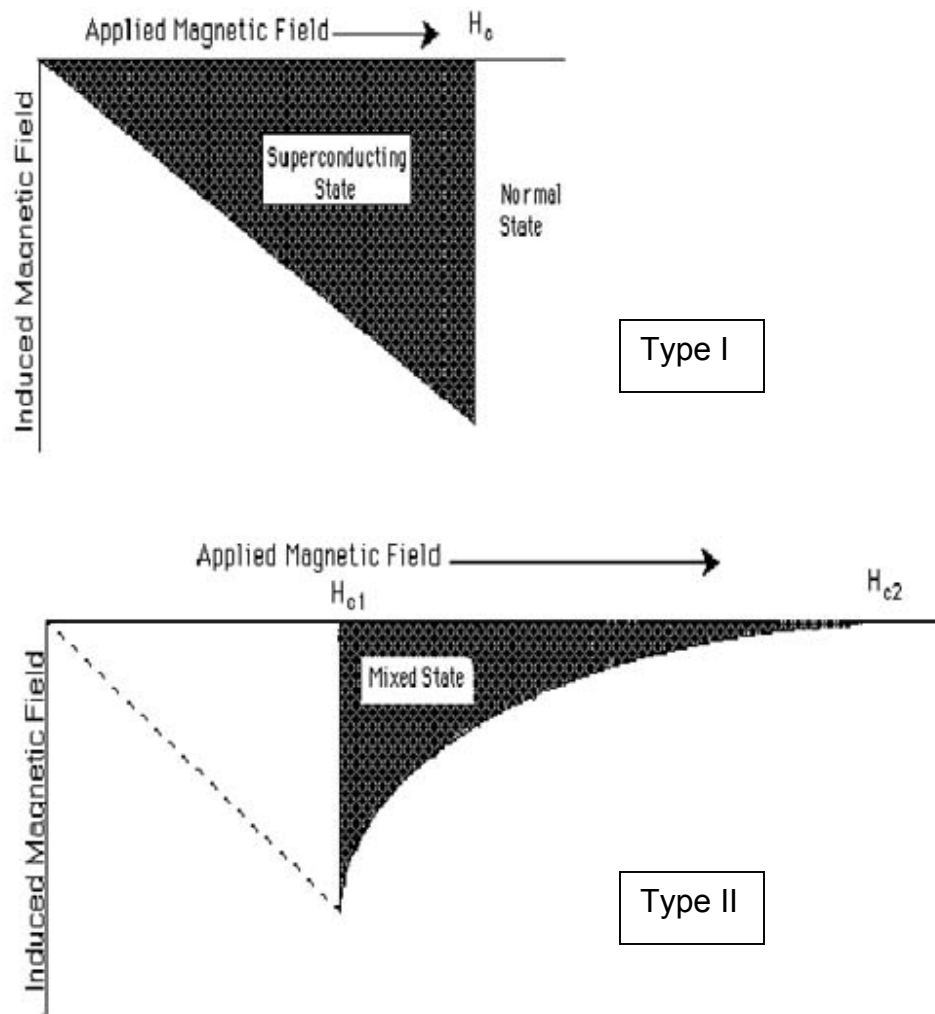


FIGURE 1.2 Comparing the different reactions to an applied magnetic field between Type I and Type II superconductors

H_{c2} is usually much larger than Type I's H_c , and allows for resistance-free current flow in higher fields. It is because of the existence of the mixed state that some Type II superconductors are being used for applications.

For Type II superconductors, J_c is not a true phase transition. Neither is it intrinsic to the material like T_c and H_{c2} are. Instead, J_c is highly dependent on the superconductor's microstructure. To understand this, first consider a block of Type II superconducting material such as that in figure 1.3.

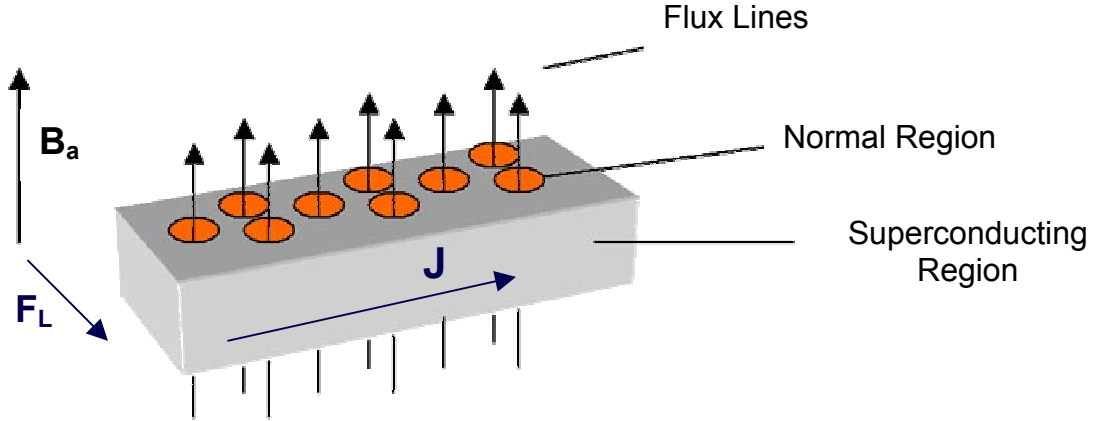


FIGURE 1.3 Type II superconductor in its mixed state, showing the presence of normal regions and flux lines

The block is in its mixed state ($\mu_0 H_{c1} < B_a < \mu_0 H_{c2}$) with a current density, J . A Lorentz force per unit volume (F_L) is produced by this current-field interaction. The force acts upon the flux line, pushing it out of the material. This results in the motion of all the flux lines, which is known as flux flow, and is a time varying magnetic field (dB / dt). Faraday's law states that

$$\nabla \times E = - dB / dt \quad (1.1)$$

In other words, a spatial varying electric field (voltage) results from the interaction between the flux lines and the transport current, and the current flow is no longer free of losses.

Zero-resistance in Type II superconductors breaks down as a result of flux motion. If the lines could be held in place, then higher currents could be transported through the material without causing flux flow. This is the strategy behind flux pinning; a technique researchers have developed to increase a material's J_c . This is accomplished by adding defects and impurities of a specific size, which act as artificial "pinning sites" that pin flux lines in place.

1.3 Superconducting Materials

Since its discovery, scientists and engineers have eagerly searched for applications that can take advantage of superconductors. H.K. Onnes himself envisioned a 10 T magnet being developed soon after his discovery of the phenomena in Hg. What he and other scientists were unaware of was that Hg, like most pure metal superconductors, is classified as Type I and has a low critical field (H_c). Hg has a transition temperature (T_c) of approximately 4 K and can withstand magnetic fields only up to approximately 40 mT. Type I superconductors are not considered useful for applications because of their low T_c and H_c limits. It was only after the discovery of Type II superconductors, and their much higher critical fields (H_{c2}), that superconducting applications became a reality.

Type II superconductivity was discovered in the 1930's but it wasn't until the early 1960's that a group of materials was found that could perform well at high magnetic fields. The Nb superconductors, NbTi and Nb₃Sn, are the most widely used superconductors today. NbTi has a T_c of ~ 10 K with an H_{c2} (4.2 K) of ~ 12 T. In addition, it has more attractive metallurgical and mechanical properties than Nb₃Sn. Nb₃Sn has a T_c of 18 K and has an H_{c2} (4.2 K) as high as ~ 28 T. It is this higher H_{c2} that makes Nb₃Sn more attractive for high field applications, despite its higher cost (10 x the price of NbTi) and a relatively complex fabrication process.

Until the mid-80's, the Nb based superconductors were considered the most suitable for applications. In fact, today they are used in more than 90% of superconducting applications. However things began to change in 1986 with the discovery of superconductivity in LaBaCuO ($T_c = 30$ K) [2]. This was the first of the now famous copper oxide superconductors that are known for their high T_c and H_{c2} values, as well as highly anisotropic crystal structures. In the following year the maximum T_c was raised twice with the discovery of YBa₂Cu₃O_{7-x} ($T_c = 90$ K) [3] and the BiSrCaCuO (BSCCO) superconductors. The two most interesting phases of BSCCO are the Bi₂Sr₂Ca₂Cu₃O_{10+δ} ($T_c = 110$ K) and the Bi₂Sr₂CaCu₂O_{8+δ} ($T_c = 80$ K) phase, known simply as Bi-2223 and Bi-2212, respectively [4]. Both YBa₂Cu₃O_{7-x} (YBCO) and Bi-2223 have H_{c2} (4.2 K) values greater than 100 T. The oxide with the highest (stable) T_c is HgBa₂Ca₂Cu₃O_x with a transition temperature of 134 K.

Unfortunately, there are many problems associated with the oxide superconductors, most of which come from their complicated and anisotropic crystal structure. As an example, the crystal structure of Bi-2223 is shown in figure 1.4. CuO₂ planes, a characteristic of HTS oxides, carry the superconducting current. To maximize J_c , it is necessary to align these planes. This is why HTS materials require a processing route that results in c-axis, or in the case of YBCO, bi-axially textured grains. In addition, HTS materials are chemically more complicated than their Nb based predecessors.

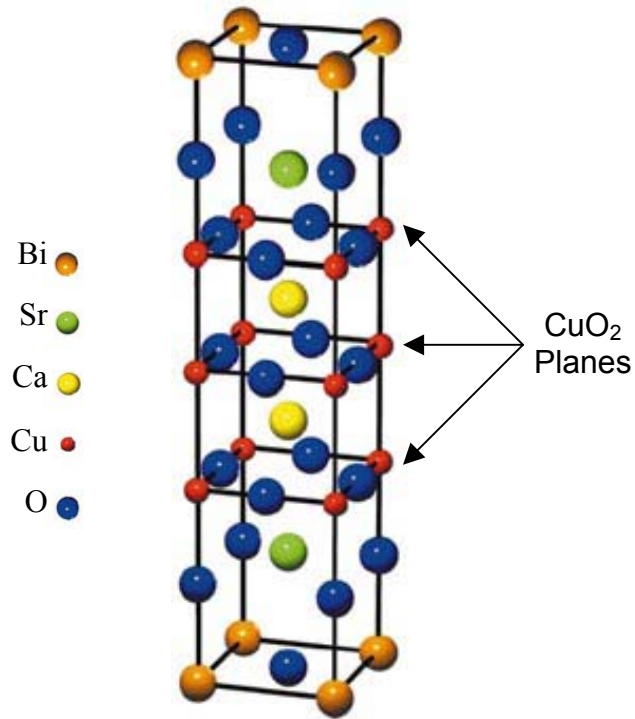


FIGURE 1.4 The orthorhombic perovskite crystal structure of Bi-2223, focusing on its three CuO₂ planes [7]

HTS materials are ceramic oxides and like many other ceramics they are brittle. To improve mechanical properties, HTS oxides are often combined with a metallic material (sheath, substrate, etc.). The metal is also needed to add stability to the conductor. Choosing a metal that fits the processing route and is chemically compatible with the superconductor is often a challenge. For BSCCO, Ag is used to make fairly long superconducting tapes; currently lengths 1 km long are available. It is chemically compatible, and with the proper mechanical deformation and heating, c-axis orientated grains can be grown. Unfortunately, the cost of Ag and the lengthy processing steps keep the price of BSCCO tape high [6]. YBCO tapes are made by epitaxially depositing films of the superconductor onto a bi-axially textured Ni substrate [5]. While this does achieve the proper grain orientation, other problems arise. First of all, YBCO cannot be directly deposited onto Ni without oxidizing it. This is why buffer layers are needed to chemically protect the oxide superconductor from the Ni substrate. While effective, it is important to note that the deposition methods involved in this process are intricate, and not yet suitable for making long length conductors.

The coherence length of HTS materials is on the order of 1 nm, much smaller than those found in LTS materials. While this allows for higher H_{c2} values, it also leads to the main drawback of high temperature superconductors. To put it simply, the coherence length describes the maximum distance between two coupled electrons, known as a cooper pair. If the paired electrons are separated by more than the coherence length, they no longer “communicate” with one another, and cease being a pair. Supercurrent cannot

flow without cooper pairs. With materials such as Nb_3Sn , which have a larger coherence length, crossing grain boundaries is of no concern. In fact, grain boundaries are known to act as pinning sites [8]. On the other hand, HTS materials are plagued with grain boundaries that can act as “weak links” to the current flow, and limit performance in a magnetic field. This is especially true for YBCO, where even a small-angle grain boundary can interrupt the flow of superconducting current.

In 2001, Akimitsu *et al.* found superconductivity in MgB_2 at 39 K [9]. This is almost twice the T_c of Nb_3Ge (23 K), the previous record holder for non-cuprate superconductors. The research community quickly raced to learn as much as they could about the material.

Much like the Nb-based superconductors, MgB_2 is a chemically simple, binary compound. This intermetallic has a hexagonal (AlB_2) crystal structure where $a = 0.3086$ nm and $c = 0.3524$ nm. The crystal is composed of alternating Mg and B planes where the graphite-like B layers are sandwiched between two Mg layers. It is believed that these B layers play an important role in the material’s superconductivity, similar to copper oxide planes in HTS materials. Figure 1.5 illustrates the MgB_2 crystal structure. Clearly, the distance between B atoms in the a-b plane is much smaller than that in the c-direction. Although this results in anisotropic properties, it is not as drastic as those found in HTS materials.

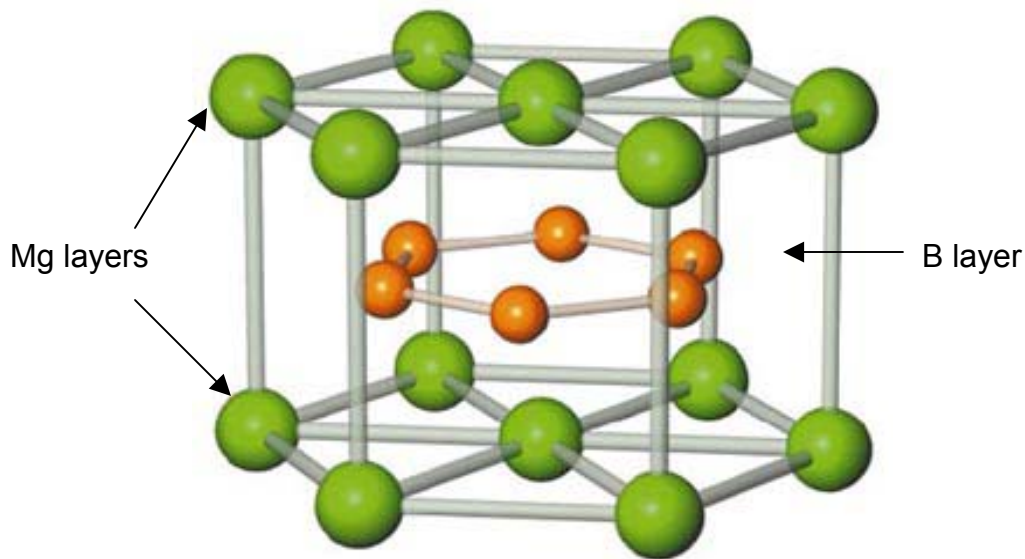


FIGURE 1.5 The hexagonal (AlB_2) crystal structure of MgB_2 [7]

As researchers learned more about MgB_2 , they quickly became aware that classifying the new superconductor would not be easy. It was found that properties, such as a linear temperature dependence of H_{c2} [10], the isotope effect [11], and a decrease in T_c (both onset and end) with increasing magnetic fields [12] suggest a conventional “low T_c ” classification. Alternatively, researchers also found MgB_2 had two properties similar to

HTS materials. First, its penetration depth (λ) varies quadratically with temperature [13] and second, as T_c is approached, there is a sign reversal of the Hall coefficient [14]. It is because of this classification difficulty that some researchers have suggested that MgB_2 might be the first of a new type of superconductor. In response, a search for similar diboride compounds began and superconductivity has been found in TaB_2 [15] and $BeB_{2.75}$ [16].

MgB_2 is currently being studied in multiple forms including bulk, wires, tapes, and thin films. Depending on the study and the fabrication method MgB_2 has an $H_{c2}(0)$ // a-b between 14–39 T, $H_{c2}(0)$ // c between 2–24 T, and an in plane coherence length, $\xi_{ab}(0)$ between 3.7 – 12 nm [18]. Although the best superconducting properties have been found in thin films, there is little hope that these procedures can be scaled up for larger applications. Instead, researchers are using the powder-in-tube (PIT) method to achieve longer length conductors. There is a wide variation in the J_c values reported but maximum J_c values of 6×10^5 A/cm² [19] and 1.0×10^7 A/cm² [20] in wires and thin films, respectively, were achieved.

The discovery of MgB_2 and its properties prompted a comparison between the new superconductor and existing materials. One of the clear differences between MgB_2 and existing HTS materials is the cost associated with their production. Both Mg and B are abundant and inexpensive, and do not require an expensive, Ag sheath, such as the one used with BSCCO tapes. Instead, low cost metals such as steel or Monel can be used as a sheath. From there, the mechanical deformation techniques used are relatively simple and well understood, which allows for future scaling up of the process. This is a problem that has kept the “second generation” YBCO coated conductors expensive. MgB_2 also has larger coherence lengths than the HTS materials, which allows for current flow that is free of weak links. Much like the Nb superconductors, grain boundaries in MgB_2 polycrystalline material has been shown to serve as effective pinning sites [21]. In addition to being chemically simple, MgB_2 also has a less complicated and less anisotropic crystal structure than HTS materials. This results in a simpler processing method because less attention is given to achieving the proper texture.

MgB_2 has the highest T_c of the intermetallic superconductors. With a transition temperature of 39 K, it is being considered for low field applications (< 3 T) such as transmission cables, transformers, and fault current limiters with temperatures ranging from 20–30 K, which is out of reach for the Nb based superconductors. This small window might prove to be a niche for MgB_2 , where it’s simple processing and low cost make it attractive.

For this to occur, MgB_2 ’s J_c in the presence of a magnetic field must be improved. Figure 1.6 depicts the highest J_c vs. field values (25 K) that have been achieved, and compares them to the Nb superconductors [18]. As you can see, there is a large difference in field dependence between the two. To alter this, researchers are looking for ways to improve MgB_2 ’s flux pinning properties.

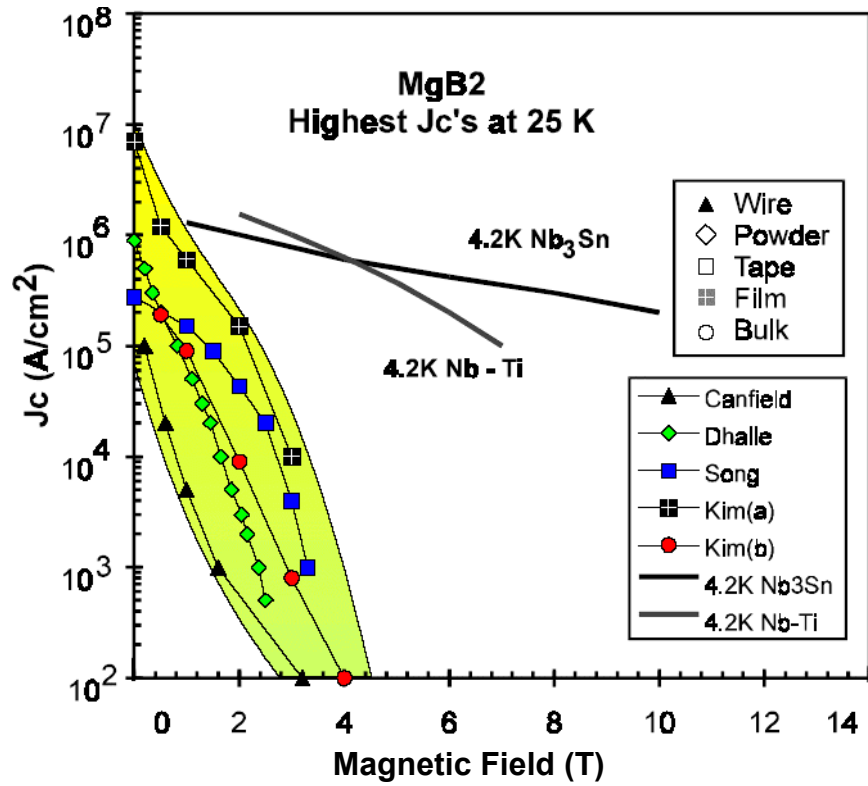


FIGURE 1.6 J_c dependence on magnetic field at 25 K for various forms of MgB_2 [18]

1.4 Scope and Objectives

The main drawback to the MgB_2 superconductor is its poor flux pinning properties. It is known that microscopic defects in a superconducting material can act as pinning sites, and thereby increase J_c . There have been a few attempts to enhance flux pinning in MgB_2 . Early on, it was shown that the defects caused by proton irradiation enhanced in-field performance [22]. Since then, thin films of O_2 doped, MgB_2 have achieved J_c values of 10^4 A/cm^2 , measured at 5 K and 14 T [20]. Although both studies focus on fabrication methods that are impractical for large-scale conductor development, they indicate that there is room for improvement by way of nano-size defects.

Several groups have been working to introduce nano-scale defects by adding precipitates to the MgB_2 matrix. This is the most effective strategy and suggests that a simple scaling up of the process is possible. Increases in J_c have been reported by a factor of 2.2 and 3.4 with the addition of WSi_2 and ZrSi_2 , respectively [23]. SEM analysis showed that the additions improved inter-grain connectivity. ZrSi_2 doped samples achieved J_c values of $\sim 5 \times 10^4 \text{ A/cm}^2$ at 4.2 K and 5 T. Currently the most

effective means of improving in-field characteristics, while still allowing the simple PIT process, is the addition of nano-size SiC particles. Addition of SiC was reported to increase J_c by a factor of 5. With 10 wt% addition of SiC, wires have been developed with J_c of 5×10^4 A/cm² at 5 K and 7.5 T [24].

Another method that has proven effective is chemical doping, where elements are either added to MgB₂ or partially substituted for Mg or B. Elements used in this strategy include Li, Na, Cu, Ag, Ca, Al, Zn, Zr, Ti, Mn, Fe, Co, C, In, Sn, and O₂. Most of these dopants showed little proof of enhanced flux pinning, and except for Al, none were proven to substitute for either element [25]. Although flux pinning was not greatly improved by doping, in some cases either densification or grain-to-grain connectivity was enhanced, which resulted in better in-field J_c characteristics. For example, In and Sn additions have resulted in the enhancement of in-field J_c performance [26]. Both elements are metals with low (< 240 °C) melting temperatures. TEM analysis showed that In was melting and filling the gaps between grains. It was speculated that this was improving the connectivity between MgB₂ grains.

It has been shown that Ti doping has improved in-field characteristics for bulk MgB₂ [27]. Ti was not an addition; instead it was partially substituted for Mg. The intent was to introduce Ti into the MgB₂ crystal. Although the substitution was unsuccessful, J_c values as high as 5×10^4 A/cm² at 5 K and 5 T were achieved. TEM studies showed that TiB₂ was forming in between MgB₂ grains [28]. TiB₂ has a hexagonal crystal structure with similar lattice parameters to that of MgB₂. It is believed that these similarities allow TiB₂ to improve intergrain connectivity within the superconductor. In addition, TiB₂ hindered grain growth, resulting in a dense, nano-crystalline microstructure. Both factors were attributed to the observed increase in J_c .

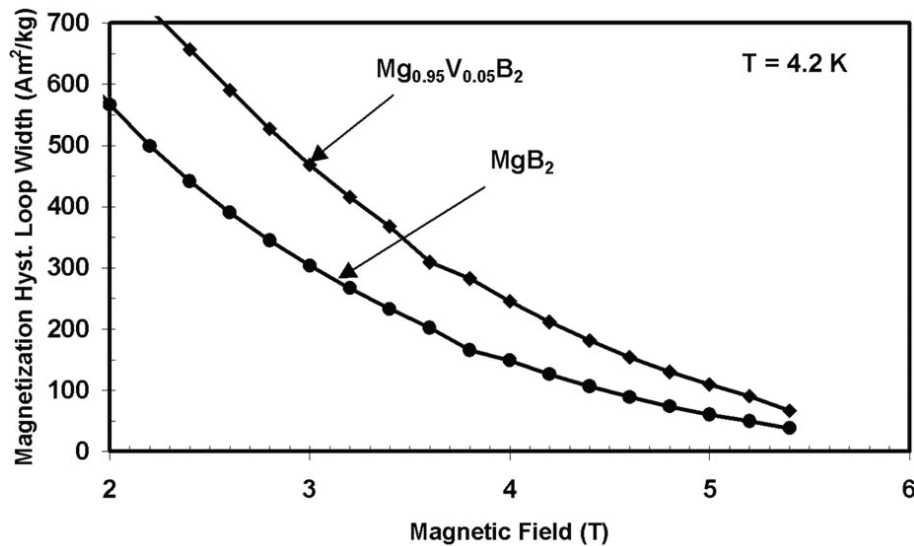


FIGURE 1.7 Hysteresis loop widths comparing V doped and undoped bulk samples [29]

Results of preliminary studies on V doped MgB_2 bulk samples have shown that V may improve J_c characteristics in a similar manner as Ti [29]. V and Ti both have similar atomic radii ($V = 1.35 \text{ \AA}$, $Ti = 1.40 \text{ \AA}$) [30] and form borides (VB_2 , TiB_2) with hexagonal crystal structures. Figure 1.7 shows that a 5 at% substitution for Mg by V improved magnetization hysteresis loop width significantly.

The studies described in this thesis were aimed at understanding how V substitution might affect phase formation, microstructure, and superconducting properties of MgB_2 both in the bulk samples and steel sheathed wires. To accomplish this, the fabrication of this new superconductor had to be better understood. Specifically, precursor powder preparation, heat treatment, and wire deformation method all had to be studied.

Note that a portion of the findings described in this study were presented at the 2003 CEC/ICMC in Anchorage, AK and have been accepted for publication in “Advances in Cryogenic Engineering (Materials)”, volume 48.

CHAPTER 2

SAMPLE PREPARATION AND CHARACTERIZATION TECHNIQUES

2.1 Sample Preparation

2.1.1. Powder Preparation

All the superconducting samples studied during this project were prepared from similar starting powders. All powders were purchased from Alfa-Aesar and had a 325-mesh particle size. Powders had the following purities, Mg 99.8 %, amorphous B 99.99 %, and V 99.5 %.

Mg was partially substituted by V to understand its effect on superconducting properties. Four compositions of powders were weighed out to obtain the nominal formula $\text{Mg}_{1-x}\text{V}_x\text{B}_2$ where $x = 0.0, 0.05, 0.10$, and 0.15 . The sets of powders were labeled based on the percentage of dopant (V) used, for example, when $x = 0.10$ the powder is referred to as “10 at%”.

In addition to the differences in composition, powders were also mixed differently, depending on what they were to be used for. This was not something planned, but came about as we improvised the steps to achieve better homogeneity. Powders used for bulk samples and groove rolled wires were mixed manually in air using a mortar and pestle. Powders used to make extruded wires, and eventually tapes, were ball milled for 48 min. at 500 rpm with 1020 carbon steel balls (2:1 / ball: powder mass ratio).

2.1.2. Bulk Samples

After mixing, the powders were pressed under 155 MPa into 0.9 g pellets, similar to those shown in figure 2.1. The pellets were approximately 5 mm thick and 12.7 mm in diameter. In an effort to contain the volatile Mg at higher temperatures, pellets were inserted into a small box or pouch made of Ni foil (Alfa Aesar, 0.002 or 0.005 in thick, 99+ % metal basis) during heat treatments. Containment is important because pellets deficient in Mg often result in the formation of higher borides, such as MgB_4 and MgB_6 , which are not superconductors. Ni was chosen to investigate the extent of the Ni/ MgB_2 reaction. If this reaction could be minimized by the proper heat treatment, then Ni could be considered an alternative sheath material to Fe or steel. Ni is an attractive sheath material because of its stability and mechanical advantages over steel.



FIGURE 2.1 Example of unreacted Mg-V-B bulk samples

2.1.3. Groove rolled wires

Due to the difficulties found using Ni during the bulk investigations it was decided that steel would be used when fabricating wires. Groove-rolled wires were fabricated using the standard powder-in-tube (PIT) method and an IRM Stanat groove rolling mill shown in figure 2.2. Approximately 3.5 g of each powder composition was used to fill 25 cm long 1020-carbon steel tubes, which were purchased from McMaster-Carr. The tubes began with a 6.35 mm outer diameter and a 0.09 mm wall thickness. After filling, steel screws were used to plug the ends of the tubes. Each tube was then groove-rolled to produce four wires, each with a different dopant percentage, all having a square cross section. The change in cross section shape was due to the formation of grooves along the wire length during fabrication. The grooves began forming as the diameter was reduced below 4 mm. Wire fabrication using the groove rolling mill became a difficult and lengthy process. On average, to fabricate the four wires, two days had to be spent manually feeding the samples into the mill, one at a time, each wire being passed through approximately 360 times. Unfortunately, even with such a slow deformation rate, samples would form cracks after about a 69 % reduction in area. This produced “wires” having cross section dimensions of about $3.15 \times 3.15 \text{ mm}^2$. It was realized that unless the cross section could be reduced, the precursor powders within the wires would not achieve the proper density, which could reduce the eventual grain-to-grain connectivity of the superconductor.



FIGURE 2.2 IRM Stanat groove rolling mill used to fabricate Mg-V-B wires

To address this problem, empty 1020 tubes were heat treated at 871 °C in Ar for 1.5 hours. This heat treatment was aimed at reducing the residual stress found in the extruded steel tubes. Samples groove rolled after this residual stress relief anneal could be deformed down to a 2.5 x 2.5 mm² cross section before breaking. This translates to an overall 80 % reduction in area. All of the characterizations conducted on groove rolled wires were of this type.

In hopes of further reducing wire dimensions, additional annealing experiments were conducted attempting to stress relieve the work hardened wires. Some consideration was given to the fact that wires, unlike the previously annealed empty tubes, are filled with unreacted precursor powders. An 871 °C anneal would cause the formation of MgB₂, and therefore would not allow for further deformation. A temperature had to be selected that was low enough to prevent the MgB₂ reaction, but high enough to relieve stress within the steel sheath. Of the work cited, none describe MgB₂ studies with reaction temperatures below 650 °C. It was decided that an anneal of at least 50 degrees below this temperature would be sufficient. Figure 2.3 [31] describes the relationship between annealing time, temperature, and the amount of stress relieved for low carbon steels. According to the plot, a 6 hour anneal at 600 °C would result in approximately an 80 % relief of stress. A 9 hour heat treatment was used to maximize the stress relief. Wire samples that underwent the initial residual stress anneal and this new intermediate, lower temperature anneal could be deformed down to a 2.05 x 2.05 mm² cross section. That is an 87 % reduction in area.

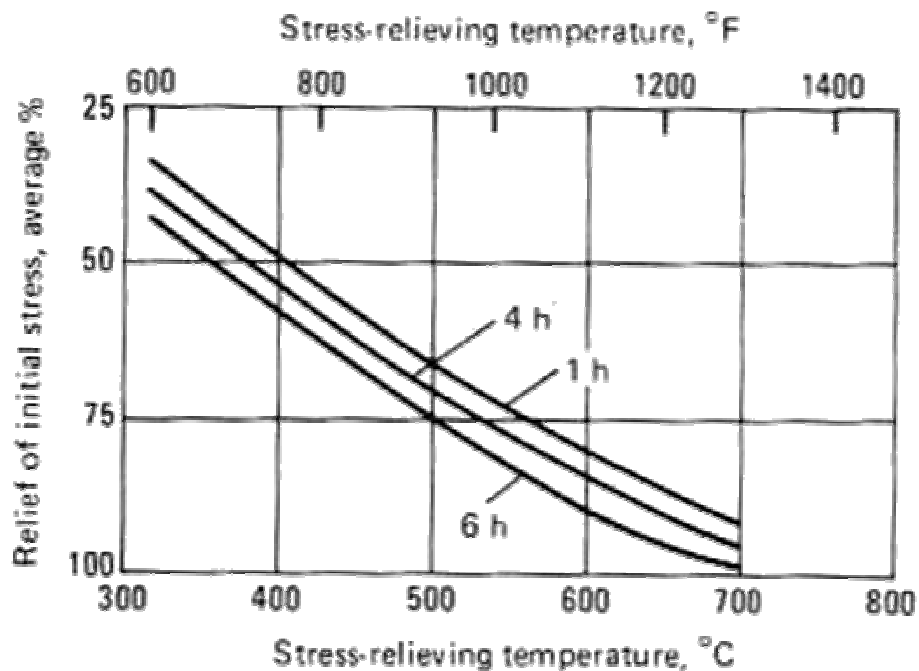


FIGURE 2.3 Relationship between time and temperature in the relief of residual stresses in steel [31]

2.1.4. Drawn Wires

The PIT method was used when developing the steel sheathed drawn wires. Approximately 3.5 g of each composition was used to fill 25 cm long 1010 carbon steel tubes purchased from McMaster-Carr. The steel tubes had an OD of 6.35 mm and a wall thickness of 0.09 mm. Prior to filling, the tubes were annealed at 871 °C (1600 °F) for 1.5 h to reduce any residual stress and allow for further deformation. One end of the tube was swaged closed, allowing for powder to be inserted into the tubes. After swaging, the tubes were cold drawn on a conventional drawing bench to a final diameter of 1.215 mm using 10 % area reduction steps. The over all reduction of area was a little over 96 %. All powder milling and wire drawing was conducted at Hyper Tech Research Inc. in Columbus, OH.



FIGURE 2.4 Drawing bench used to fabricate Mg-V-B wires

2.2 Heat Treatments

The heat treatment portion of these studies was conducted to optimize the reaction process of MgB_2 and to understand how that reaction was affected by the partial substitution of Mg with V. The plan was to try a broad range of heat treatments, beginning with long reaction times and eventually moving on to shorter reaction times, with the peak temperature ranging from 800 to 900 °C. Heating routines began from ambient temperature, increasing at 400 °C/hour until the peak reaction temperature was reached. After reaction, samples were furnace cooled back to ambient temperature. Figure 2.5 is a schematic showing the furnace configuration used. The majority of this study was done with bulk samples because of the flexibility of preparation and characterization. This information would then be used when developing and fine-tuning a heating routine suitable for V doped MgB_2 wires and tapes.

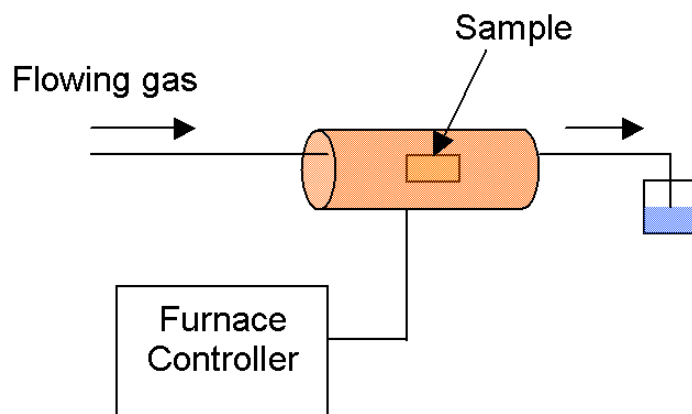


Figure 2.5 Schematic of the furnace system used

2.2.1. Bulk Samples

In the process of searching for an optimum heat treatment many different routines were investigated. The heat treatment study can be separated into two phases. In the first set of experiments, four pellets, one of each composition, were reacted using heating routines with peak reaction temperatures varying from 800 to 900 °C for 1 or 2 hours. Samples were wrapped in Ni foil (Alfa Aesar, 0.002 or 0.005 in thick, 99+% metal basis), placed in an alumina boat, and inserted into a furnace. All heat-treatments during the first set of tests were carried out in flowing Ar.

After reviewing the results of the initial experiments, the reaction process was modified. Reaction time was reduced from 1 hour to shorter times that included 0.5, 0.3, and 0.2 hours. Temperature was restricted to 800 and 850°C and all experiments were carried out in flowing 5% H / Ar. Samples were wrapped in 0.005 in thick Ni foil.

2.2.2. Groove rolled wires

Reactions of the groove rolled samples were conducted soon after the second set of bulk heat treatments. One of the goals of the experiments was to optimize the heat treatment of the wires using a similar approach as that described for the bulk samples. The plan was to study a few different reaction temperatures between 750 and 850 °C for short reaction times ranging from 0.1 to 0.5 hours. These studies were expected to produce results with greater reproducibility than those found in the bulk studies because there was no need to complicate the process by wrapping the samples in Ni. All heat-treatments were carried out in flowing 5% H / Ar on 6 cm long sections cut from the stock wires.

2.2.3. Drawn wires

Drawn wires were heat treated with reaction temperatures varying from 700 to 800 °C all for 0.5 hours. The ends of the samples were pinched closed and all heat treatments were conducted in flowing 5% H / Ar. All samples were approximately 5 cm in length.

2.3 X-ray Diffraction (XRD)

An x-ray diffractometer is a characterization tool that can be used to determine different material properties including crystal structure, grain orientation, changes in lattice parameters, or distinguishing between phases in a multi-phase material. To understand how a diffractometer works it is first necessary to review Bragg's Law and x-ray diffraction.

$$n\lambda = 2 d_{hkl} \sin(\theta) \quad (2.1)$$

Bragg's law states that for x-rays with a single wavelength (λ), a relationship exists between the spacing of atomic planes (d_{hkl}) and the angle (θ) at which diffracted x-rays will constructively interfere with each other. A simple way to understand how this law helps to characterize materials is to realize that different crystalline materials have different planar spacing; therefore diffraction will constructively interfere at different angles depending on the material. If this interference is plotted against twice the angle, then the location of the constructive peak will change depending on what material is being examined. Now realize that within a three dimensional crystal, many planes of atoms exist, so one material will have many peaks, but all located at an angle specific to the distance between those planes. This plot is known as an x-ray diffraction pattern and can be used to identify materials. Figure 2.6 shows an XRD schematic.

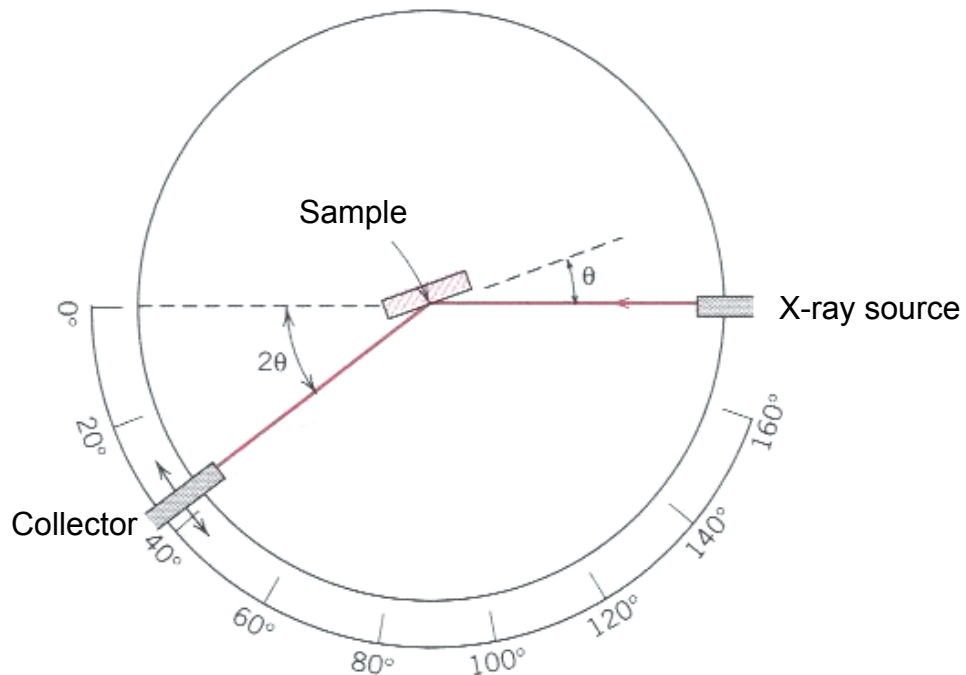


FIGURE 2.6 Schematic of XRD system [32]

XRD was used primarily for phase analysis. Since secondary phases such as MgO and MgB₄ form during the MgB₂ reaction, a diffraction pattern of the samples would have peaks from all three materials, overlapping one another. It was necessary to identify which peaks belonged to which materials and to monitor how the relative peak intensities were affected by heat treatments and dopant concentration. Large concentrations of impurities such as MgO and MgB₄ take away from the total superconducting volume, which limits current flow.

2.4 Environmental Scanning Electron Microscope (ESEM) and Energy Dispersive Spectroscopy (EDS)

The scanning electron microscope (SEM) is widely used in the analysis of a specimen's microstructure and phase composition. One reason for its popularity is the availability of high resolution, over a wide range of magnifications. The environmental scanning electron microscope (ESEM), which was used in this study, differs from the traditional SEM by not requiring a high vacuum in the sample space during operation. This allows non or poorly conducting samples (such as many HTS materials at room temperature) to be examined without the need of a conductive coating. It also makes switching between samples easier.

An SEM works by bombarding a specimen with a finely focused electron beam that scans across its surface. This beam interacts with a region at the sample surface and produces secondary electrons, backscattered electrons, auger electrons, and also characteristic x-rays. A different detector is used for each emission, depending on what type of information is needed.

Secondary electrons have relatively low energies (~10 eV) and are emitted from a volume close to the surface, near the beam impact area. These electrons carry information regarding the specimen's surface topography. Backscattered electrons carry higher energies (5-40 keV) and penetrate the specimen farther than secondary electrons. Backscattered electrons transmit information on the specimen's chemical composition, crystal orientation, and due to an interaction with secondary electrons, surface topography as well.

Characteristic x-rays are produced when the electron beam knocks an electron from an atom's inner shell, leaving a vacancy. When an outer shell electron fills this vacancy, thereby reestablishing ground state, the x-rays that are released are characteristic of the excited atom. Detection of these x-rays is accomplished by an energy dispersive spectrometer (EDS), which is a solid-state device that distinguishes between x-ray energies. This provides compositional information of various phases for elements with atomic weights greater than that of Na (~23 amu).

2.5 Superconducting Quantum Interference Device (SQUID)

The superconducting quantum interference device (SQUID) can be used to measure very small changes in magnetic field. A SQUID incorporates the use of Josephson junctions, which is based on the tunneling phenomena. A Josephson junction consists of two superconducting materials separated by a thin insulating material (10 – 20 Å) that acts as a “weak-link” between the superconductors. A SQUID is a closed loop of superconducting material with one or more of these weak-links. Figure 2.7 shows a schematic of a superconducting ring with two Josephson junctions. The critical current (I_c) of the weak-link is less than that of the superconducting ring, so the current that can flow through the ring (without resistance) must be limited to the weak-links' I_c . This results in Cooper pairs with reduced momentum, and thus very long wavelengths.

To see the importance of these changes consider a scenario where the superconducting ring is cooled in absence of any magnetic field (ZFC) below its critical temperature (T_c). A magnetic field applied perpendicular to a ring *without* weak links will induce a current in the ring to exactly cancel out the applied field, leaving the interior of the loop free of any net flux. On the other hand, a ring whose I_c is limited by weak-links will reach a point where it can no longer match the applied field. Therefore, the electron pairs will feel the effect of the magnetic field, which induces a phase difference in the current flowing around the ring. This phase difference is proportional to the flux of the applied magnetic field. It can be shown that the induced current variation in the ring corresponds to a flux change of one fluxon ($\sim 2 \times 10^{-7}$ gauss cm²), making the squid a very sensitive magnetometer.

Magnetization measurements can be used to estimate critical current density (J_c). This is accomplished by applying Bean's critical state model [33], which relates critical current density (J_c) to magnetization hysteresis loop width (ΔM) and the circulating current loop diameter (d).

$$J_c = 2\Delta M/d \quad (2.2)$$

The error associated with this model is dependent on a specimen's geometry and the interconnectivity of its superconducting grains. The Quantum Design Magnetic Property Measurement System (MPMS), which incorporates a SQUID in its design, was used to measure T_c and magnetic hysteresis of superconducting bulk samples. To accomplish this, small pieces of approximately the same mass (15.6 mg) and volume (~ 18.8 mm³) were taken from bulk samples for measurement.

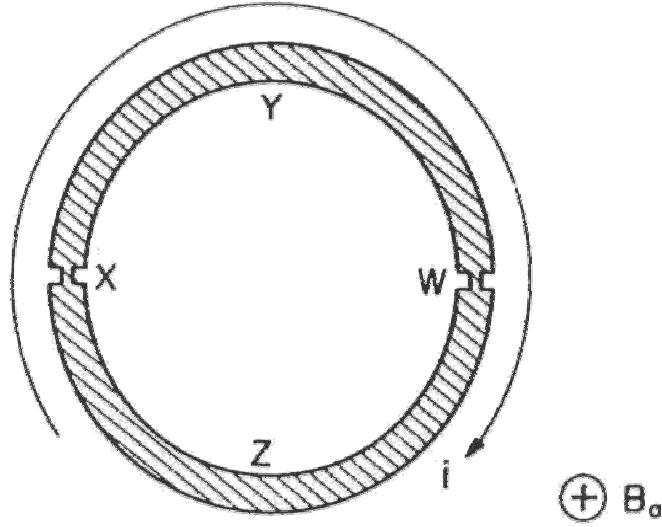


Figure 2.7 Superconducting ring with two Josephson Junctions [34]

2.6 Transport Measurements

Magnetization measurements were used primarily to characterize the superconducting properties of bulk specimens. This proved effective due to the fact that both SQUID sample preparation and the actual measurements were relatively easy. Unfortunately, magnetization measurements are not sufficient for characterization of polycrystalline superconducting material. The hysteresis loop width (ΔM) measured is composed of two signals, one from the intragranular current and the other from the intergranular (transport) current. In other words, large values for ΔM do not necessarily translate to high transport current values. This is why short sample critical current measurements were used to characterize the superconducting properties of wires.

All measurements were conducted at 4.2 K, using the four-point method described in figure 2.8. The average sample length was 45 mm, with an average tap length of 20 mm. A voltage criterion of $1 \mu\text{V}/\text{cm}$ was used. It was hypothesized that the resistance of the steel sheath was causing an increase in temperature during measurements. This increase in temperature would lower I_c , and therefore make the measurement unreliable. To minimize this heating, thin copper wire was wound around the ends of samples. Current leads were then soldered directly to the copper windings. The transport critical current density (J_c) was calculated by dividing the measured I_c by the cross sectional area of the superconducting core, obtained from optical or ESEM micrographs.

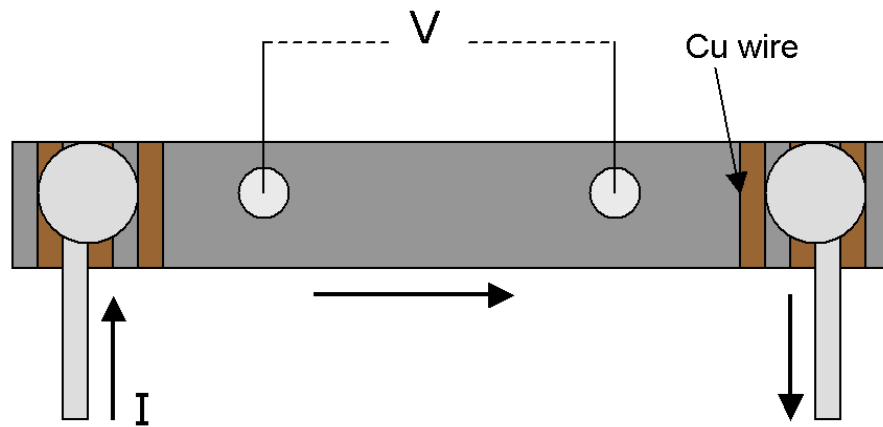


FIGURE 2.8 Schematic of 4-point method used to measure I_c

CHAPTER 3

INVESTIGATION OF BULK SAMPLES

3.1 Initial Results

Results from the first set of bulk experiments showed that a reaction was occurring between the MgB_2 pellets and the Ni foil. After reaction, pellets were often “stuck” to the foil and covered in a chalky, gray layer. These gray layers were sometimes accompanied by holes in the Ni foil where the pellets and foil came in contact. In addition to this reaction with Ni, samples were usually brittle, and in some cases, cracked into many pieces and scattered throughout the nickel box. This made it impossible to distinguish the pellets from one another. Finally, after reaction, the surface of many pellets appeared white, which was evidence that despite the Ar atmosphere, MgO was forming. Examples of these various results can be seen in figure 3.1. All of these issues made it close to impossible to see any improvements made by the V substitution or the various heat treatments.

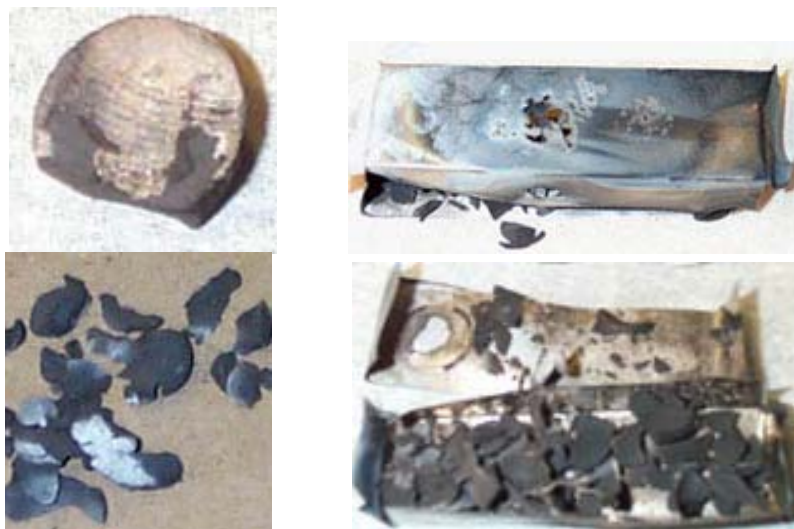


FIGURE 3.1 Examples of problems encountered during bulk sample fabrication

X-ray diffraction analysis was conducted to verify the MgO formation and an MgB_2 / Ni reaction. Figure 3.2 is an MgB_2 diffraction pattern obtained from prereacted MgB_2 powder, which is commercially available from Alfa-Aesar. The pattern can be used as a reference because it contains all of the peaks for MgB_2 in this 2θ range. The two most intense peaks are those belonging to the 100 and 101 planes, which are located at 33.5° and 42.5° , respectively. Figure 3.2 also contains a diffraction pattern taken from an undoped pellet, heat-treated at 850°C for 1 hr.

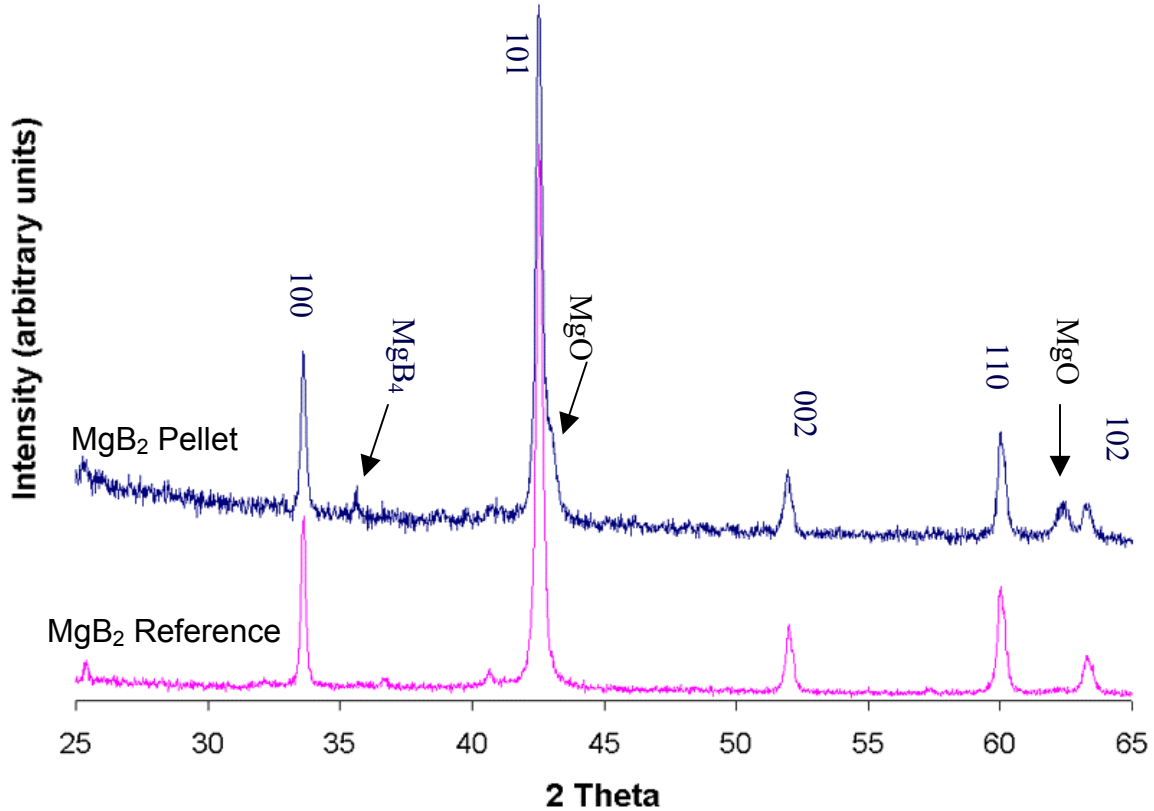


FIGURE 3.2 XRD patterns taken from Bulk sample and Alfa Aesar, prereacted MgB_2 powder

In addition to the peaks indicative of MgB_2 , the bulk sample's XRD pattern also contained additional peaks, which are found in MgO and MgB_4 patterns. Although samples had been covered by Ni and reacted in Ar, the presence of MgB_4 and MgO was somewhat expected. A tightly sealed pellet would be needed to retain Mg vapor completely. In addition, all of the powders were mixed in air, which may have been a source of oxygen. One must realize that any "loss" of Mg, even due to the formation of MgO , would make the samples Mg deficient, which would lead to the formation of MgB_4 . The goal of the heat treatment optimization was to minimize these impurities and to see how the presence of V affected the optimum formation temperature for MgB_2 . This information would later be used in developing a heating routine for V doped MgB_2 wires, which was one of the goals of the project.

In order to reduce the amount of oxygen present during reaction, future experiments were conducted in a background atmosphere of 5 % H / Ar. This reduced the visible signs of oxidation on the surface of the pellets, but XRD analysis of the surface showed that MgO was still present. It was believed that the presence of a sheath material would greatly reduce the likelihood of MgO formation on the surface of an MgB₂ wire core. Since this was what our heat treatment would eventually be used for, it was decided that samples used for characterization (XRD and magnetic hysteresis) would be taken from the center of the pellet.

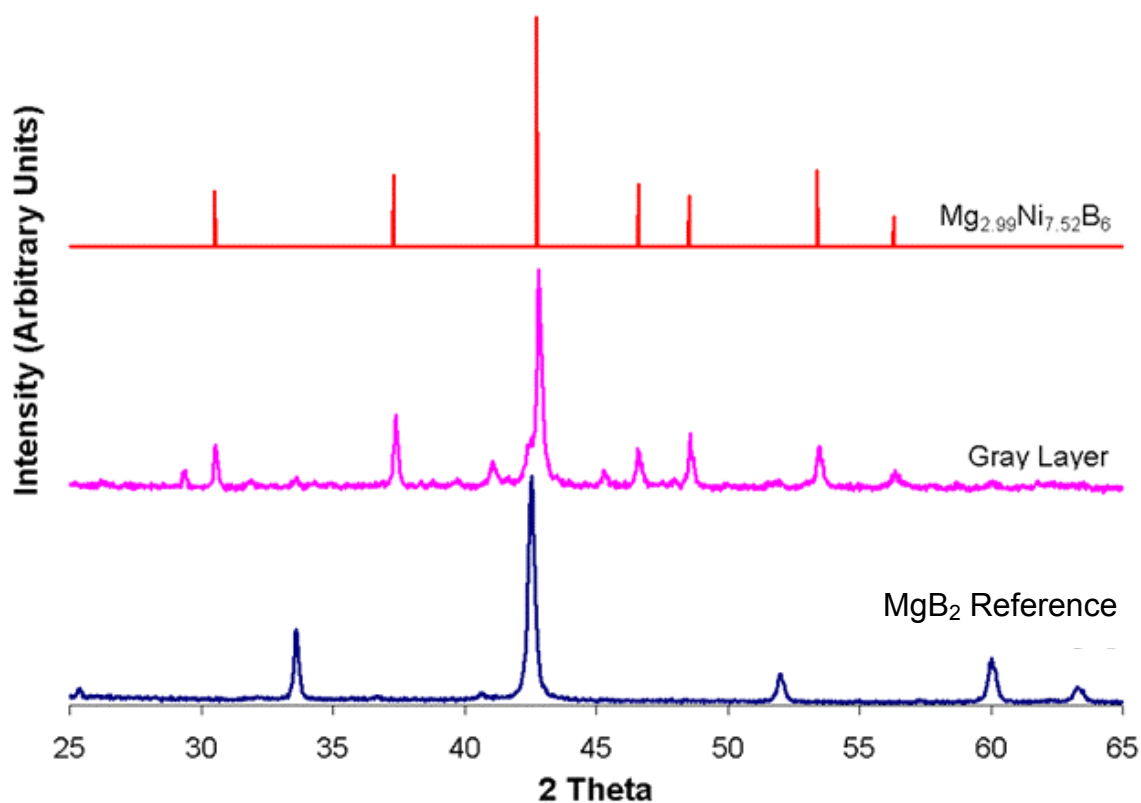


FIGURE 3.3 XRD patterns comparing the gray layer found on the surface of pellets with an MgB₂ and Mg_{2.99}Ni_{7.52}B₆ reference

In an effort to identify the composition of the gray exterior layers, samples from the outer portion of the pellets were analyzed by XRD. An example of the XRD pattern found is shown in figure 3.3 along with the pattern from the pre-reacted MgB₂ powder, which can be used as a reference of MgB₂ diffraction pattern. It can be seen that the gray layer's pattern does not match that of MgB₂, and therefore is composed of some other material. After searching through the XRD database, a compound was found having peaks with the proper intensity and position as those found. The pattern belonged to the compound Mg_{2.99}Ni_{7.52}B₆ and is also displayed in figure 3.3.

Based on the initial results, it was proposed that during heat treatment, Mg, B, and Ni were reacting to create a compound. It was noticed that this only occurred at locations where the pellet and foil came into contact. This reaction would lead to a hole forming in the foil, which would allow the Mg vapor to escape, thereby leading to the formation of MgB_4 . To address this issue, the thickness of the Ni foil was increased from 0.002 to 0.005 in. In addition, pellets were positioned in a way to minimize contact with the Ni foil. This modification, along with the switch to 5 %H / Ar gas, eliminated many of the initial problems found on the surface of reacted pellets. Unfortunately, samples would still often crack into many small pieces, although finding scattered pieces was rare.

3.2 Results

3.2.1. Phase purity by XRD

When examining x-ray diffraction results it was important to monitor the peaks belonging to impurity phases such as MgO and MgB_4 . In the 2-theta range investigated, common MgB_4 peaks were located at 35.7° and 38.9° while MgO peaks could be found at 42.9° and 62.3° . The remaining peaks, 33.5° , 42.5° , 51.9° , 59.9° , and 63.2° all belonged to MgB_2 . Diffraction peaks belonging to V compounds were not expected, due to the small concentrations added.

Figure 3.4 shows a set of diffraction patterns taken from undoped pellets, reacted for 2 hours at various peak reaction temperatures. As the reaction temperature increases to 900°C the MgB_4 peaks appear and the MgO peaks become more prominent. Also, there is no indication that 800°C is the lowest reaction temperature that will yield samples with low impurities.

Heat-treatments were also carried out with a shorter reaction time of 1 hour. In addition, a 700°C heat-treatment was conducted to identify the minimum reaction temperature. These results are shown in figure 3.5. Just as before, it seems as though impurities increase with reaction occurring at 900°C , although the peaks are not as prominent with the shorter reaction time. Also it seems as though samples reacted at 700°C begin to show the signs of increased impurity formation.

Figure 3.6 shows the diffraction patterns taken from a set of V doped bulk samples heat-treated at 800°C for 1 hour. There seems to be no increase in impurities with increasing dopant substitution. In fact, other than the MgO peaks, samples appear to be relatively free of impurities.

Based upon the apparent success at 800 °C for 1 hour, it was selected for the reaction temperature when investigating shorter reaction times. Figure 3.7 contains the diffraction patterns taken from undoped bulk samples reacted at 800 °C for times ranging from 0.2 to 1 hour. Again, all samples have low concentrations of impurities, with the “purest” pattern belonging to the 0.3-hour sample.

In a similar manner as before, a set of V doped samples, all heat treated at 800 °C for 0.3 hours, were analyzed by XRD and their results compared in figure 3.8. Although the undoped (0 at%) sample still appears to be impurity free, there is a clear degradation of phase purity as dopant percentage is increased.

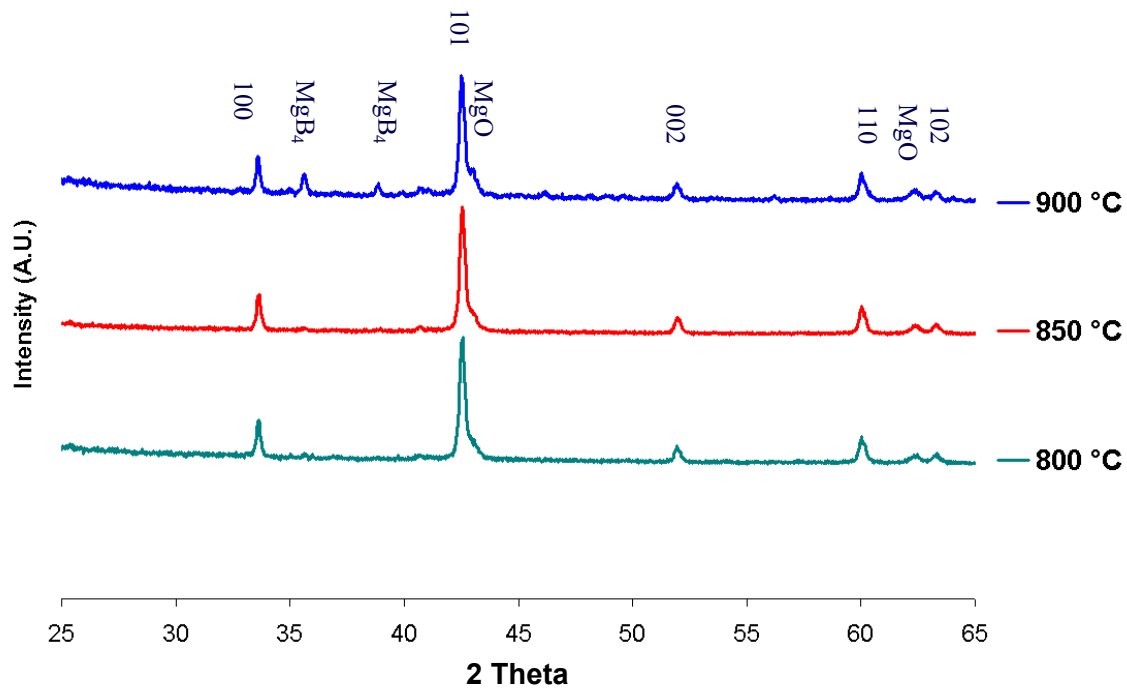


FIGURE 3.4 XRD patterns of undoped (0 at%) bulk samples, reacted for 2 hours, at various temperatures

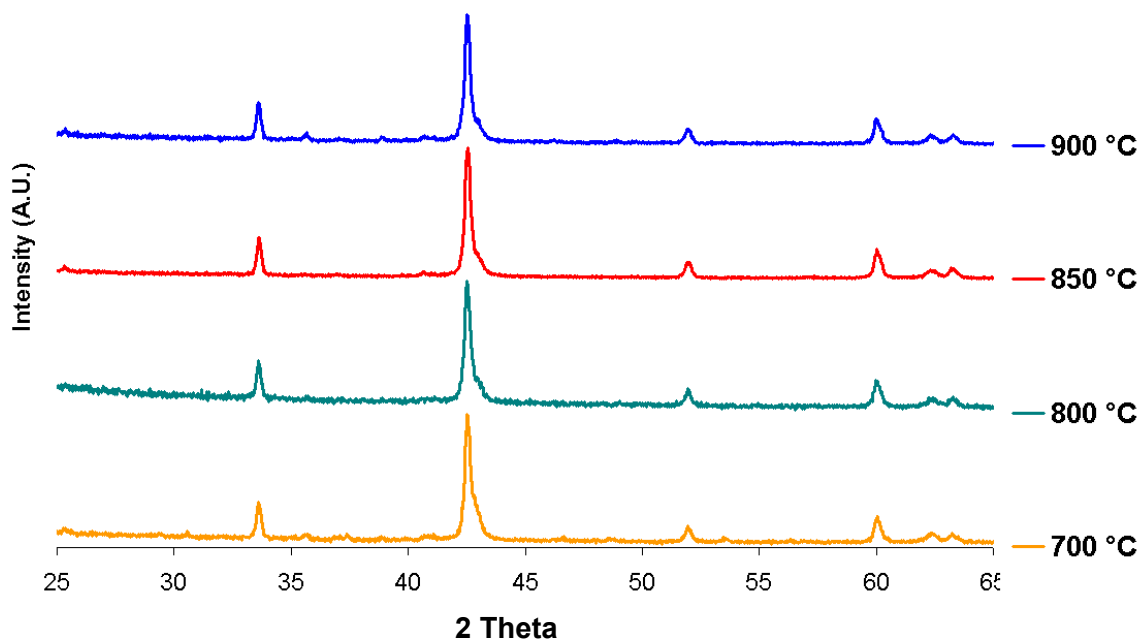


FIGURE 3.5 XRD patterns of undoped (0 at%) bulk samples, reacted for 1 hour, at various temperatures

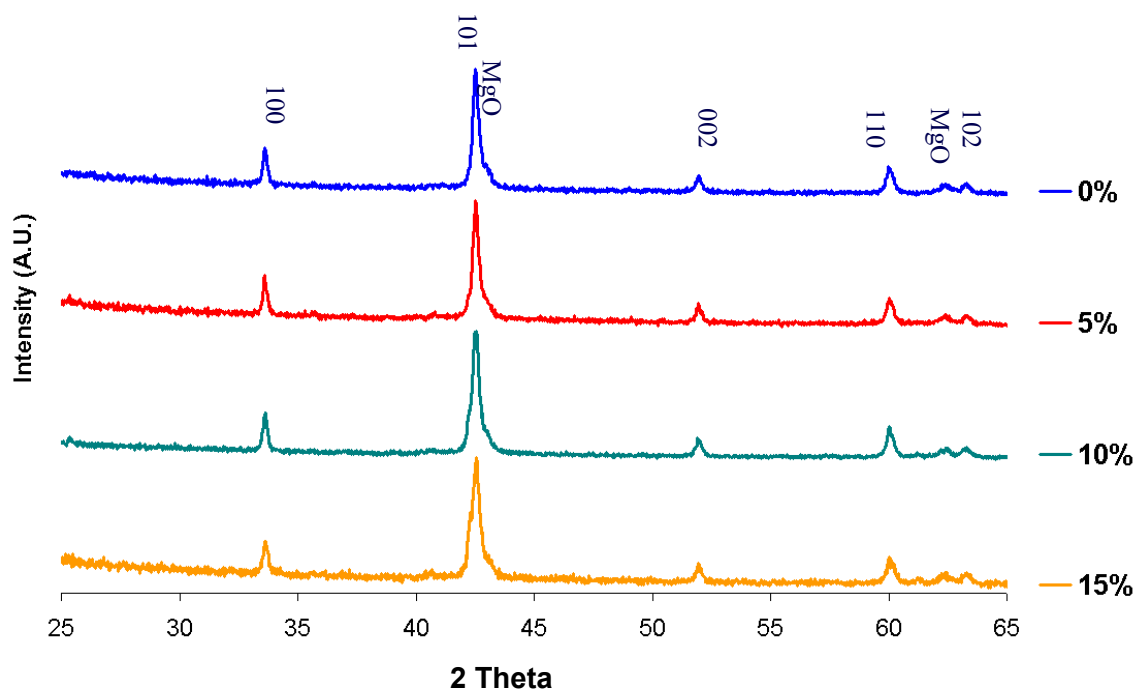


FIGURE 3.6 XRD patterns of bulk samples reacted at 800 °C for 1 hour, with increasing V dopant

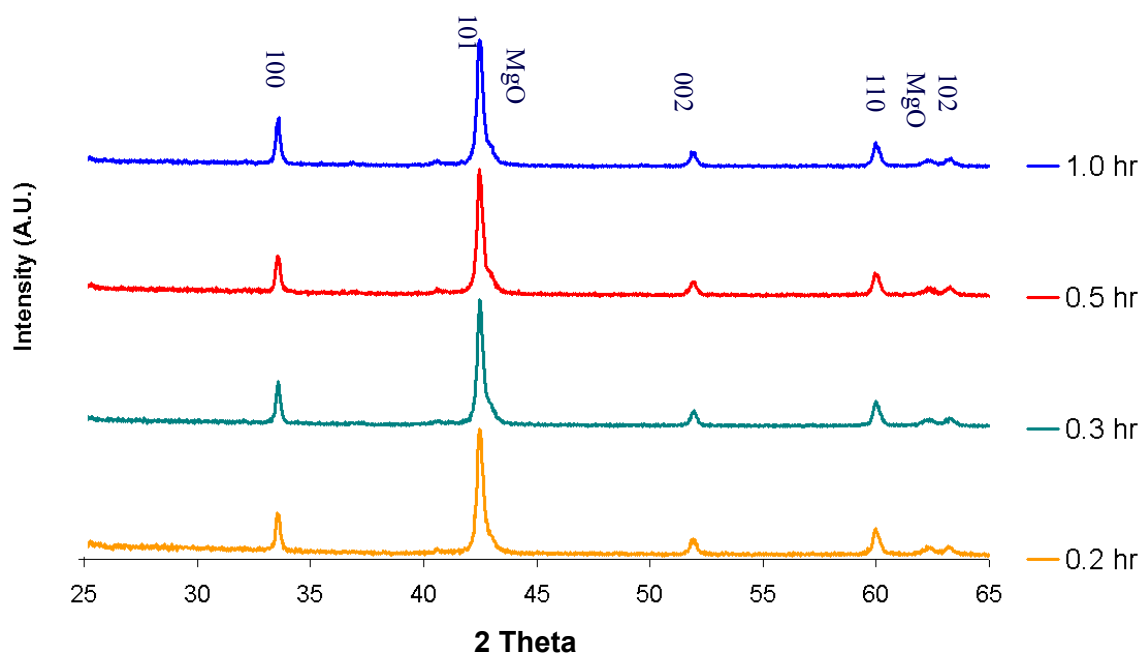


FIGURE 3.7 XRD patterns of undoped (0 at%) bulk samples, reacted at 800 °C for various reaction times

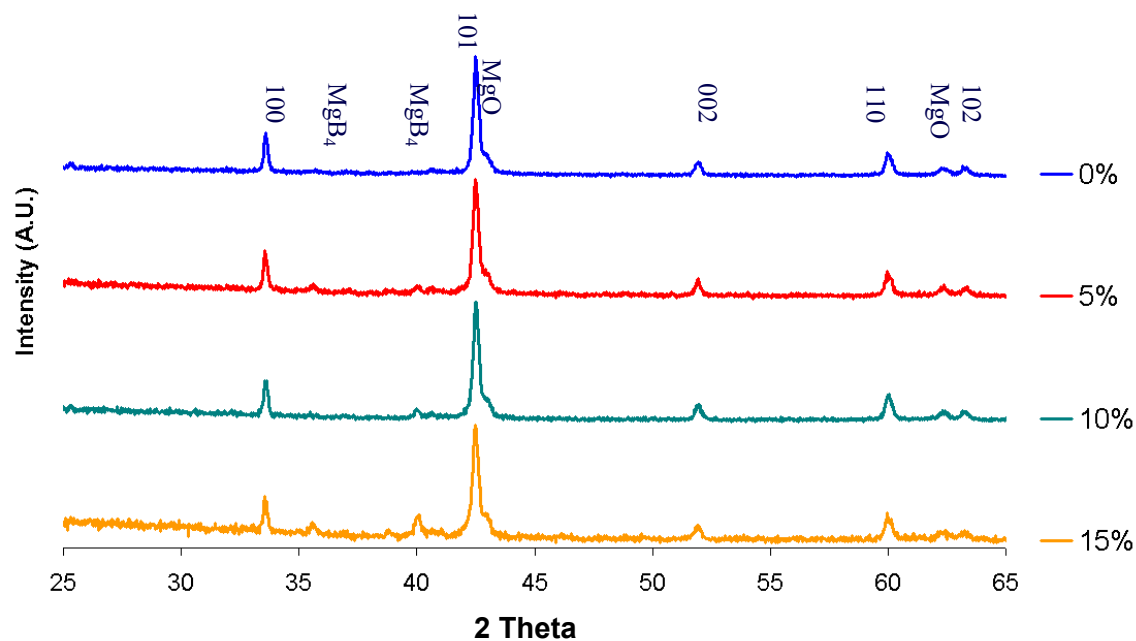


FIGURE 3.8 XRD patterns of bulk samples reacted at 800 °C for 0.3 hour, with increasing V dopant

3.2.2. Superconducting Properties

Due to the difficulties involved in performing transport measurements on bulk samples, magnetization hysteresis measurements were necessary to monitor any improvements made by the V substitution or the varying heat treatments. As discussed in the previous chapter, the hysteresis loop width, ΔM , is directly proportional to critical current density (J_c) as described in Bean's critical state model [30]. A typical T_c measurement of V doped, bulk MgB_2 is shown in figure 3.9. This measurement was made in absence of an applied magnetic field. As can be seen from the plot, the onset of transition occurs at 37 K.

Due to the low concentration of impurities found during XRD analysis, magnetization hysteresis measurements were made on samples of each composition, heat-treated at 800 °C for 1 hr. Their loop widths (ΔM) are plotted against applied magnetic field in figure 3.10. Overall, there are only small differences between the different samples, especially in the case of the undoped (0 at%) and the 5 at% measurements where the lines overlap. This suggests that there was little improvement due to such a small substitution. On the other hand, there is a noticeable improvement found in the 10 at% sample, and then a sudden drop off with the 15 at% sample

In an effort to investigate heat treatments with shorter reaction times, samples were also reacted for 1, 0.5, and 0.2 hours at 800 °C and 850 °C. Results from these measurements are shown in figure 3.11 and 3.12, respectively. One can see that there is a general trend of increasing values for ΔM with decreasing reaction time. While this is apparent in both studies, it is more prominent in the samples reacted at 850 °C.

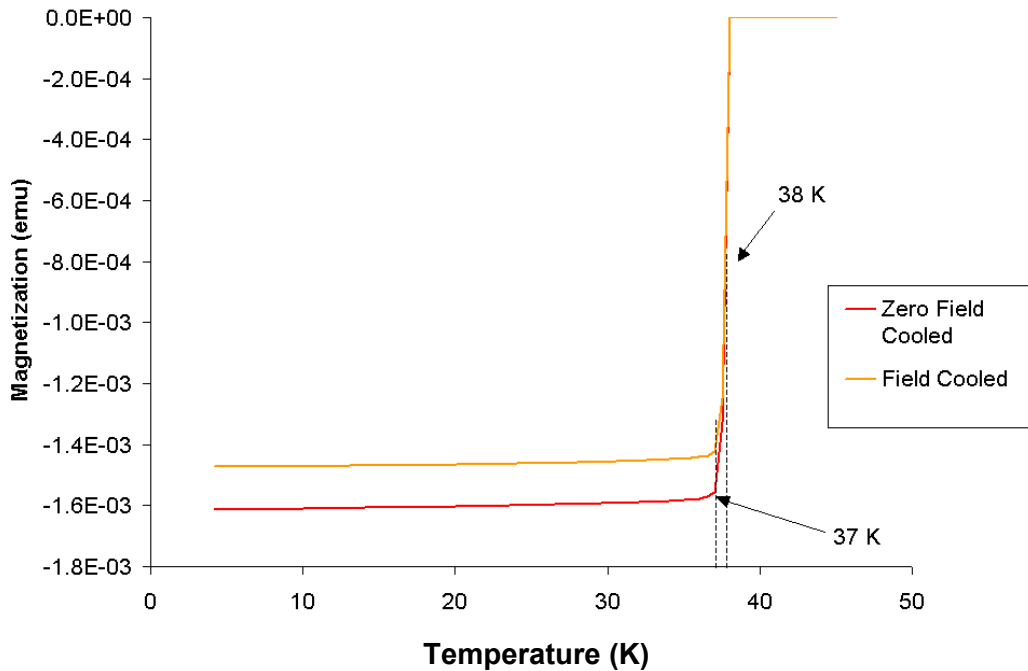


FIGURE 3.9 Magnetization versus Temperature for 10 at% V doped bulk sample showing a T_c onset of 37 K

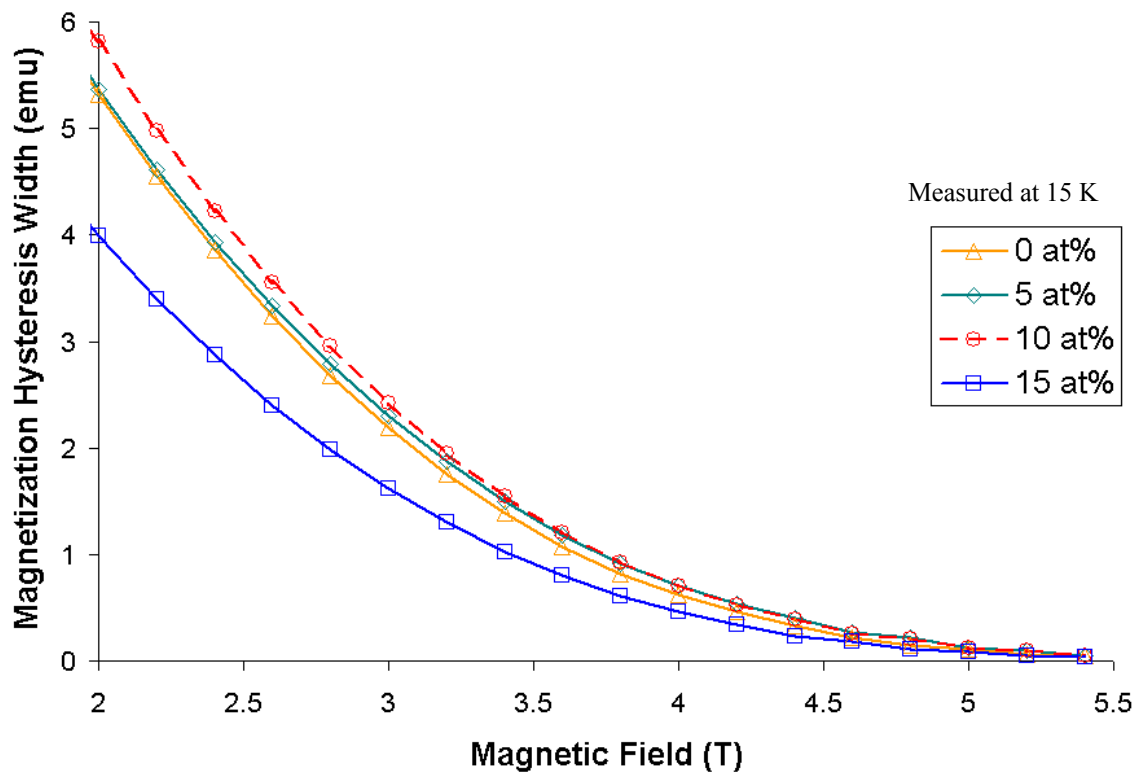


FIGURE 3.10 Magnetization hysteresis width of bulk samples reacted at 800 °C for 1 hour, with increasing V dopant

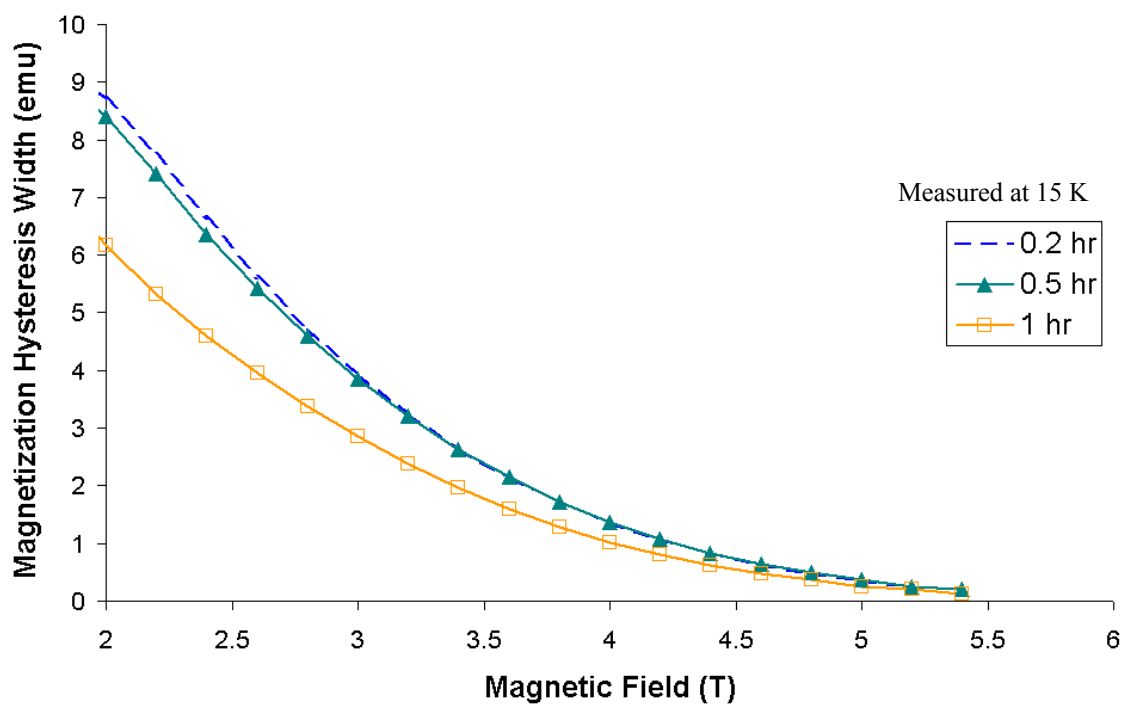


FIGURE 3.11 Magnetization hysteresis width of 10 at% V doped, bulk sample reacted at 800 °C for various reaction times

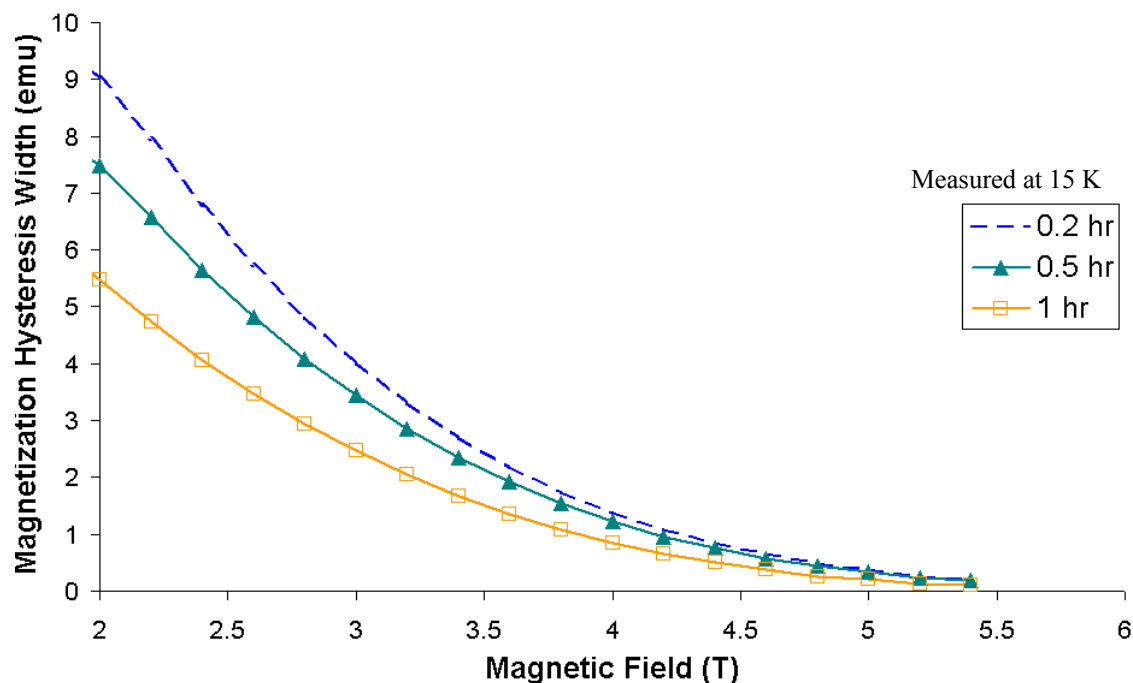


FIGURE 3.12 Magnetization hysteresis width of 10 at% V doped, bulk sample reacted at 850 °C for various reaction times

3.3 Conclusions

It was found that during reaction, physical contact between Mg-V-B pellets and Ni foil results in the formation of the compound $\text{Mg}_{2.99}\text{Ni}_{7.52}\text{B}_6$. Also, XRD analysis shows that impurities in bulk samples, reacted for 1 hour, can be reduced with reaction temperatures between 700 and 850 °C. These studies show that optimization of reaction temperature and duration is critical to achieve phase purity in MgB_2 samples.

Figure 3.6 compares XRD patterns for samples reacted at 800 °C for 1 hour. There is little difference in impurities as dopant concentration is increased. If V is not entering the MgB_2 matrix, samples should be Mg deficient, which usually leads to the formation of higher order borides, such as MgB_4 or MgB_6 . The fact that higher borides did not form, suggests that the samples are not suffering from Mg deficiency and that V is substituting for Mg.

XRD patterns for samples reacted at 800 °C for 0.3 hours are compared in figure 3.8, which depicts a clear increase in MgB_4 ($2\theta = 38.9^\circ$) with increasing V concentration. The MgB_4 increase is not due to a change in Mg oxidation, whose most prominent peak ($2\theta = 42.9^\circ$) does not vary with dopant concentration. It is more likely that the increase in MgB_4 is related to the increasing dopant substitution, as stated above.

The main difference between the two studies was a decrease in reaction duration from 1 to 0.3 hours. The results suggest that longer reaction is necessary to incorporate V into the samples. As a reminder, during heat treatments the maximum reaction temperature was attained at a fast heating rate of 400 °/hour.

Figure 3.10 compares magnetization loop widths of V doped samples reacted at 800 °C for 1 hour. The loop width increases with dopant concentration until the 10 at% dopant level and then there is a dramatic drop for 15 at%. This indicates that 10 at% substitution may be the optimum dopant level. Figures 3.11 and 3.12 focus on 10 at%-doped samples reacted at 800 and 850 °C, respectively, for shorter reaction times. Both plots show an increase in magnetization loop width with decreasing reaction times.

Although the original intent of the studies on bulk samples was to optimize heating routines to reduce impurities, it appears as though the impurities are accompanied by an improvement in performance. This is not to suggest that the impurities are causing the improvements, which is possible, but improbable. Instead, it is more likely that shorter reaction times suppress grain growth, which results in a higher grain boundary density. Similar to Nb based superconductors, grain boundaries in MgB_2 have been shown to act as pinning sites [21]. A microstructural investigation of grain growth is needed to confirm this.

CHAPTER 4

INVESTIGATION OF GROOVE ROLLED WIRES

4.1 Results

4.1.1. Sheath / Core interface

Wire samples fabricated by groove rolling did not have a smooth, round outer surface. Instead, as the fabrication method suggests, four grooves were formed along the length of the wires which forced the otherwise round conductor into a square like shape. Figure 4.1 is an optical image of the axial cross section of a typical conductor. Samples, such as the one in figure 4.1, that underwent the pre-deformation residual stress anneal, could be rolled down to a $2.5 \times 2.5 \text{ mm}^2$ cross section. Only after an intermediate stress anneal could the wires be reduced to the $2.05 \times 2.05 \text{ mm}^2$ cross section without cracking.

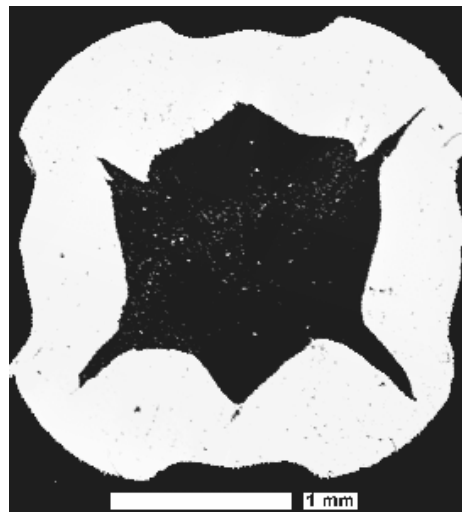


FIGURE 4.1 Axial cross section of groove rolled wire having $\sim 2.5 \times 2.5 \text{ mm}^2$ outer dimensions

As seen in figure 4.1, cracking generally occurred at the corners of the square where material was being pinched off by the grooves. In addition, groove rolled wires suffered from non-homogeneous sheath thickness. Due to these fabrication problems, fewer samples were heat treated than was originally planned. All of the groove rolled wires

investigated were reacted for 825 °C for 0.1 hour, a heat treatment based on the results of the bulk heat treatment optimization studies. Although difficult to see in this image, no reaction between MgB_2 and the steel sheath was found. Finally, the average cross-sectional area of the core was measured to be approximately 2 mm².

4.1.2. Transport Measurements

Although wires of all four compositions were developed, only 0, 5, & 10 at% doped samples resulted in reproducible I_c measurements. The difference was most likely due to errors made during fabrication rather than the V substitution. Also, groove rolled wire samples were measured without the assistance of copper windings. The advantage of using copper winding was discovered later, when measuring the conventionally drawn wires. Heating due to the resistance of the steel sheath may have lowered the I_c of all the wires fabricated, but due to the limited deformation, groove rolled wires had a thicker sheath which resulted in difficulties during I_c measurement. The maximum I_c measurements attained for the three compositions reacted at 825 °C for 0.1 hr, as well as their calculated J_c values, are displayed in figure 4.2. Maximum I_c measurements are plotted due to reproducibility issues and the low number of samples measured.

The trend in the maximum I_c measurements resembles the results of bulk magnetization measurements, where there is little difference between the undoped and 5 at% samples, but an enhancement when the substitution is increased to 10 at%. Note that the I_c value for 10 at% (660 A) in figure 4.2 is a limitation of the measuring system. Precise I_c could not be measured due to excessive heating at the current lead contacts that quenched the sample.

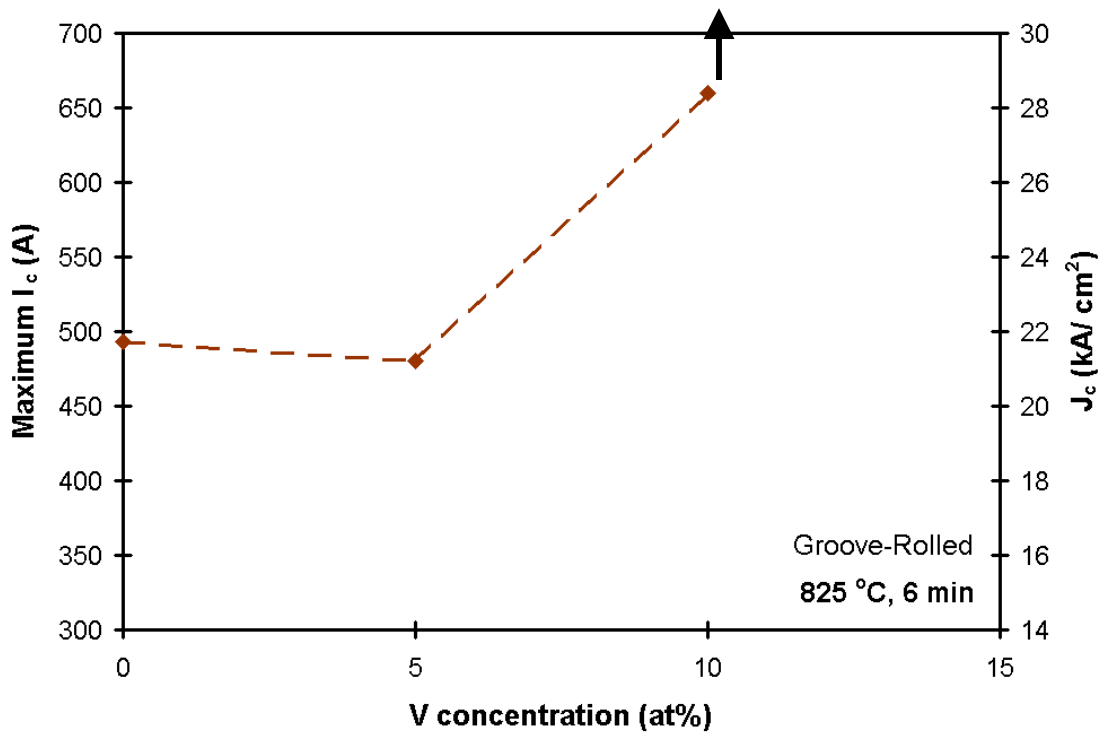


FIGURE 4.2 Maximum I_c (4.2 K) values measured for varying dopant concentrations in groove rolled wires

4.2 Conclusions

Groove rolling is not an effective processing route when attempting to develop dense, steel sheathed, MgB_2 wires. Due to the nature of the deformation technique, 4 grooves are formed along the length of the conductor, resulting in square wire with a $2.5 \times 2.5 \text{ mm}^2$ cross section. It is difficult to reduce wires below this cross section without the formation of cracks. Due to the difficulties encountered during fabrication, long lengths of wires were not formed. This reduced the number of samples that could be investigated, which limited the heating routines examined. All groove rolled wires were reacted at 825°C for 0.1 hour.

Despite processing limitations, significant I_c results were achieved in groove rolled samples. All wires measured, regardless of dopant concentration, had I_c values greater than 490 A. Unfortunately, due to the lack of densification, J_c was limited to $2.4 \times 10^4 \text{ A/cm}^2$. Although the 15 at% wire produced unreliable I_c , results from the lower dopant concentration samples ($x = 0.0, 0.05$, and 0.10) showed a steady increase in I_c with increasing dopant concentration.

CHAPTER 5

INVESTIGATION OF DRAWN WIRES

5.1 Results

5.1.1. Sheath / Core interface

The wire fabrication process proved to be straightforward and several meters of unreacted wire were fabricated. Although each wire had a different dopant concentration, they were physically indistinguishable from each. This was an important parameter that was missing from all other sample types, but it was believed that this type of sample homogeneity was necessary to isolate the effects of V substitution and varying heat treatments.

Figure 5.1 shows the axial cross section of a typical reacted, undoped drawn wire. After drawing, wires of all compositions had an outer diameter of 1.215 mm and an inner core area of approximately 0.44 mm^2 . The outer surface appeared round and smooth, as did the inner superconductor / metal interface. There also appeared to be no reaction between the core and sheath for all dopant levels.

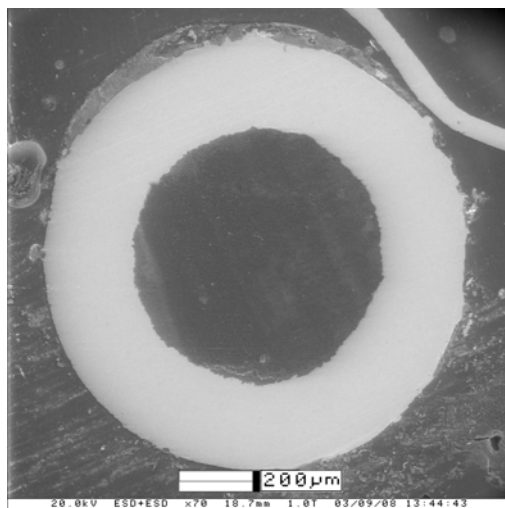


FIGURE 5.1 Axial cross section of a cold drawn wire, having an outer diameter of 1.215 mm

Figure 5.2 shows the longitudinal cross-section of reacted, drawn wires. There is no indication of sausaging in any of the wires examined. Also, there is no measurable difference in the cross-sections of the wires along the lengths. The figure contains micrographs of all four compositions beginning with the undoped wire (a) and progressively increasing the dopant level until reaching the 15 at% sample (d). While all samples are primarily composed of the darker, MgB_2 phase, one can see a gradual increase of brighter particles as the dopant content is increased. The composition of these particles is investigated in the next section.

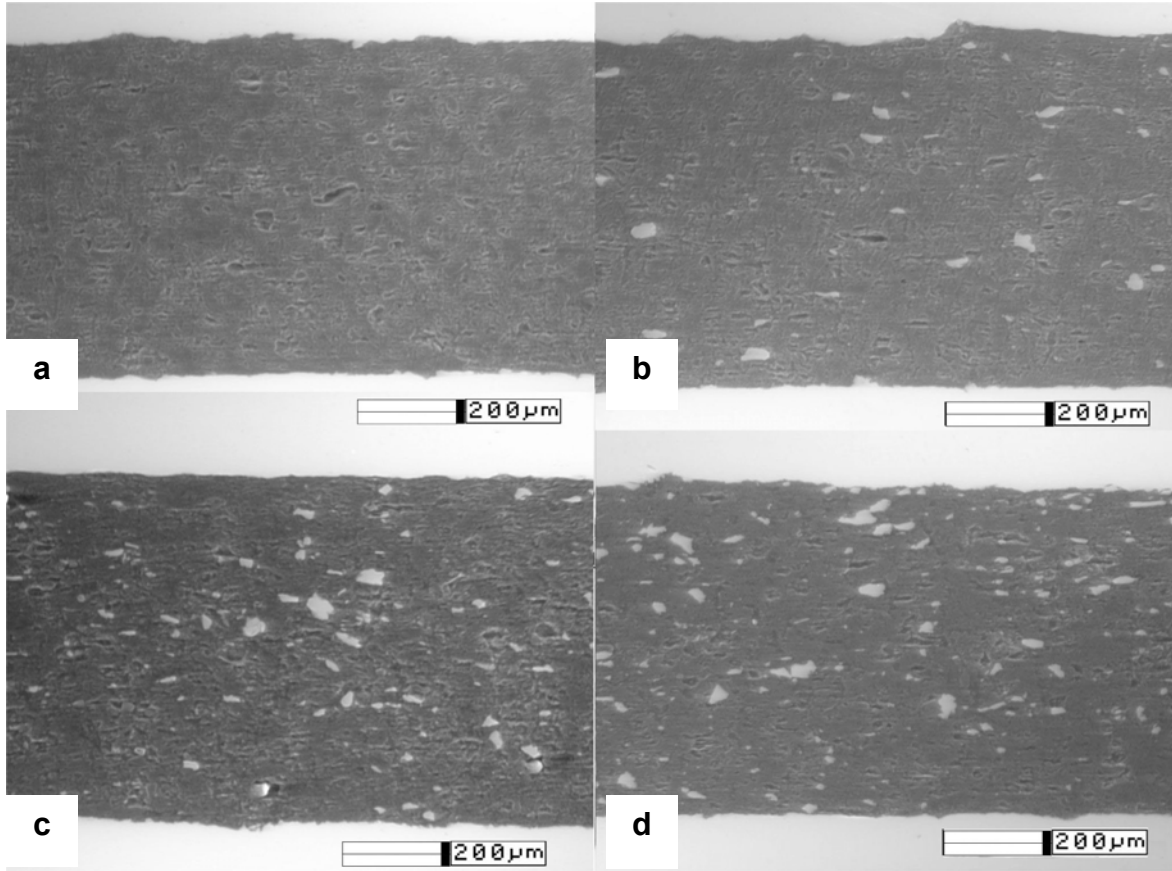


FIGURE 5.2 Longitudinal cross sections of cold drawn wire, with varying V dopant concentrations (a) $x = 0.0$, (b) $x = 0.05$, (c) $x = 0.10$, (d) $x = 0.15$.

5.1.2. Microstructure and Dopant Distribution

Figure 5.3 is an electron micrograph taken from the core of a 5 at% doped wire. This was recorded at a higher magnification to better explain the differences found in the sample's microstructure. This wire was reacted at 700 °C for 30 minutes but the bright particles seen in the micrograph were visible in all doped samples, no matter how they were heat-treated. Particles could often be classified by their shapes, which was either long and thin (a) or round and bulky (b). EDS spot analysis was used to characterize the different phases present. An example of the results found is shown in figure 5.4.

Before analyzing the results found during the EDS analysis, it is important to note that prior to the analysis, samples were polished using conventional silicon carbide-grinding paper. Although the samples were washed with ethanol after polishing, the grinding paper could have left behind Si, while Fe and Mo were most likely introduced by the sheath during either sample polishing or powder milling due to the porosity of the superconducting core. Further investigations are needed to fully understand the origin of these elements.

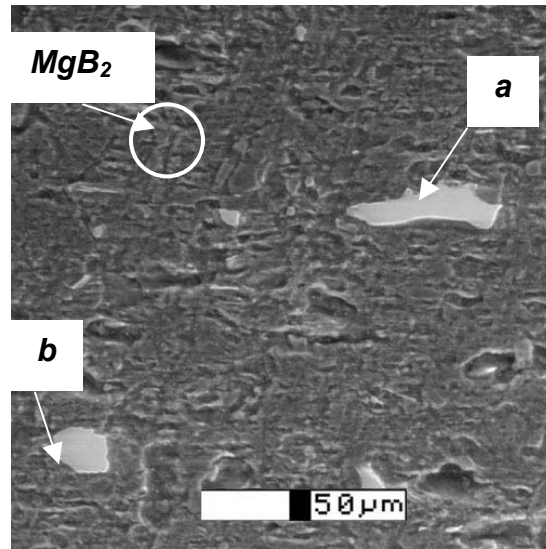


FIGURE 5.3 Micrograph taken from the core of a 5 at% doped wire, where secondary phases have been labeled

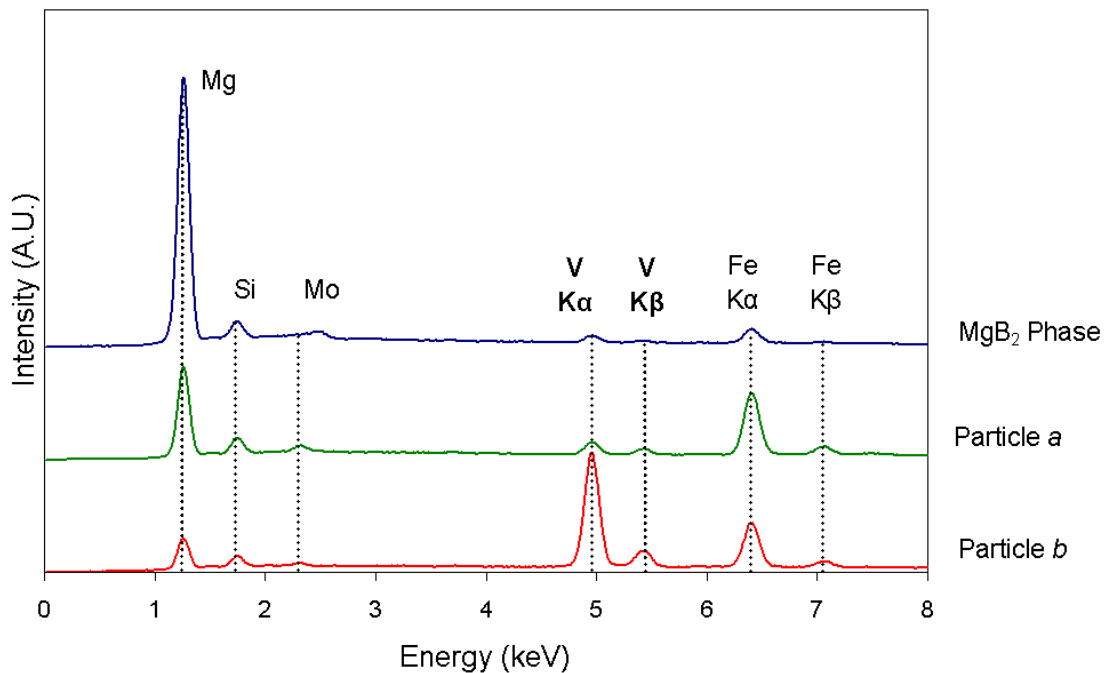


FIGURE 5.4 EDS spectra of phases in Figure 5.3

The main background phase is labeled as MgB_2 phase in figure 5.4. The most prominent peak is Mg and is located at approximately 1.3 keV. There is no B peak present because EDS can only be used to identify elements having a larger atomic weight than that of Na. Although much smaller, there are also Si, Fe, Mo, and V peaks are present.

The plot for Particle *a* contains the same peaks as those seen in the main phase, but the peak ratio between Mg and Fe is much different. In the main phase the intensity of Fe was approximately 7 % of Mg's whereas in Particle *a*'s spectra the ratio is closer to 70 %. A similar shift of intensities is found for Particle *b*, but this time between V and Mg. The V / Mg ratio increases from less than 5 % in the MgB_2 scan to more than 300 % in Particle *b*.

5.1.3. Transport Measurements

From the beginning, the I_c measurement portion of this study has been plagued by reproducibility problems, which are most likely due to the current transfer issues through the resistive Fe sheath. In the first phase, values would vary anywhere between 660 A and 22 A, independent of heat treatment or dopant content. Every effort was made to control variables both in the processing of the wires and in the measurement.

In particular, one modification to the measurement procedure improved the range in I_c . The current vs. voltage plot of two I_c measurements is shown in figure 5.5. Both samples are 15 at% doped wires reacted at 700 °C for 30 minutes. Although there was no difference in their fabrication process, there is an order of magnitude difference between their I_c values. It can be seen when examining the 30 A plot that there is an initial increase in voltage when the current is applied, this is due to the resistance of the steel sheath. It was thought that this resistance could be causing heating at the current leads, which would in turn heat the superconducting core and greatly reduce I_c . To address this problem, copper wire was wound around the ends of the samples before the current leads were soldered. This technique produced I_c results ranging between 660 A and 300 A. This was an improvement, but still a very wide range of values.

Figure 5.6 depicts the maximum I_c found for each composition (0, 5, 10, and 15 at%) and the three reaction temperatures. Even when the values are narrowed down to their maximums there is still a large variance in the results. Although nothing concrete can be said regarding optimum dopant level or heating routine, a few interesting points are clear. First of all, it appears as though no combination of V % or reaction temperature is spoiling the samples. As can be seen from the plot, almost every combination produced samples with a maximum critical current density (J_c) of at least 10^5 A/cm^2 . In fact, one of the 15 at% doped samples, which according to the previous bulk magnetization data appeared to be beyond the saturation level, has the highest measurable I_c values at 660 A. This specific wire was heat treated at 700 °C for 30 minutes, a heat treatment that also produced the highest maximum I_c values for the pure and 5 at% doped samples.

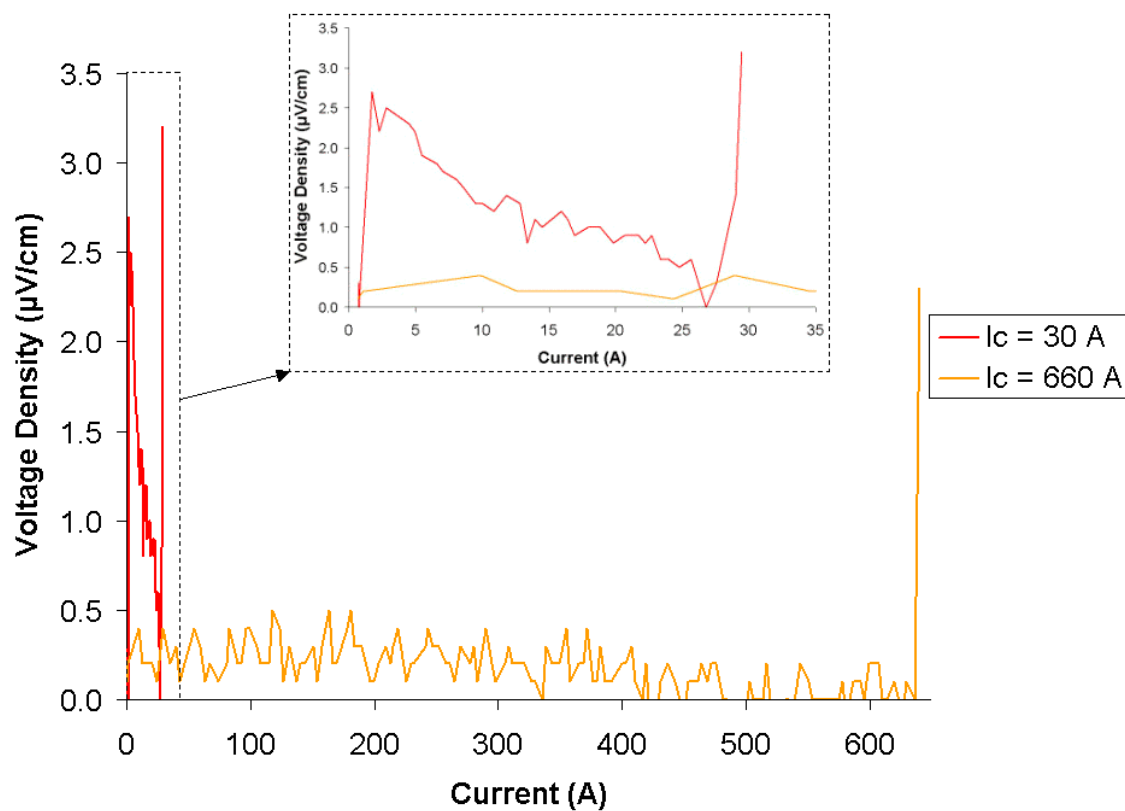


FIGURE 5.5 V vs. I plot showing the differences encountered when measuring I_c (4.2 K) in drawn wires

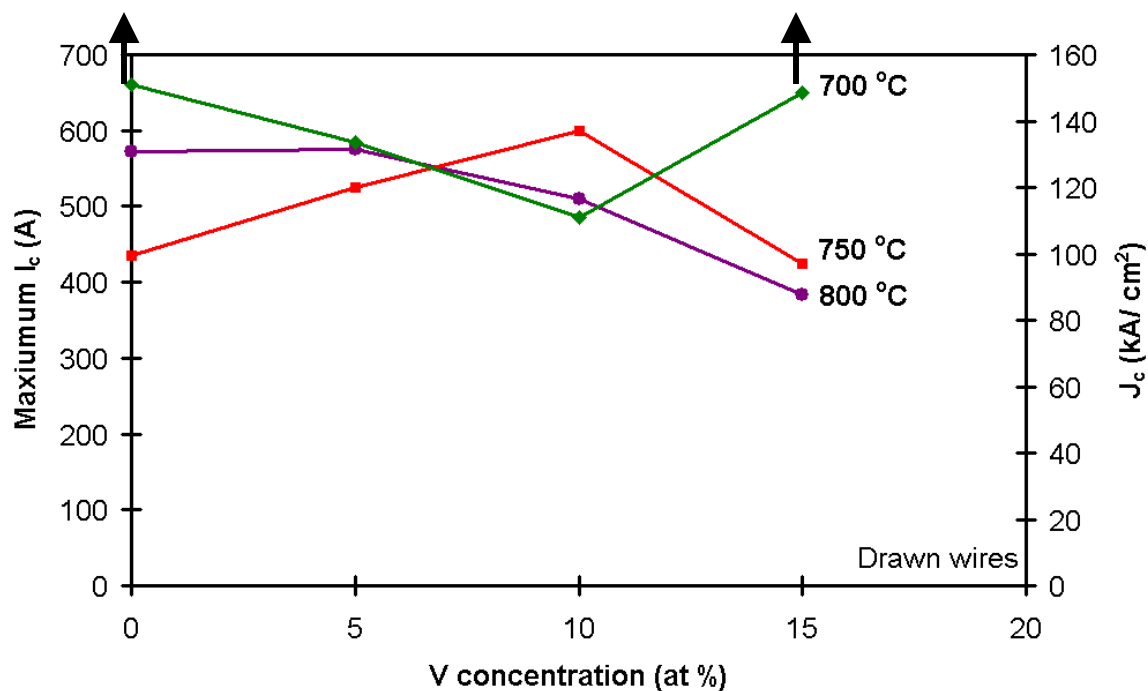


FIGURE 5.6 Maximum I_c (4.2 K) values measured for varying dopant concentrations and heat treatments in drawn wires

Although figure 5.6 is useful when investigating the upper limits of measured I_c values, it does not reflect the large spread in data found. An example of the variation found in I_c measurements can be seen in Figure 5.7, which contains all I_c measurements (between 300 – 600 A) for the 10 at% doped samples. The average I_c for this dopant content varies between 375 - 435 A with a standard deviation between 74 – 80 A, depending on the heat-treatment. The average I_c of all 69 measurements was found to be 438 A, with a standard deviation of 92 A.

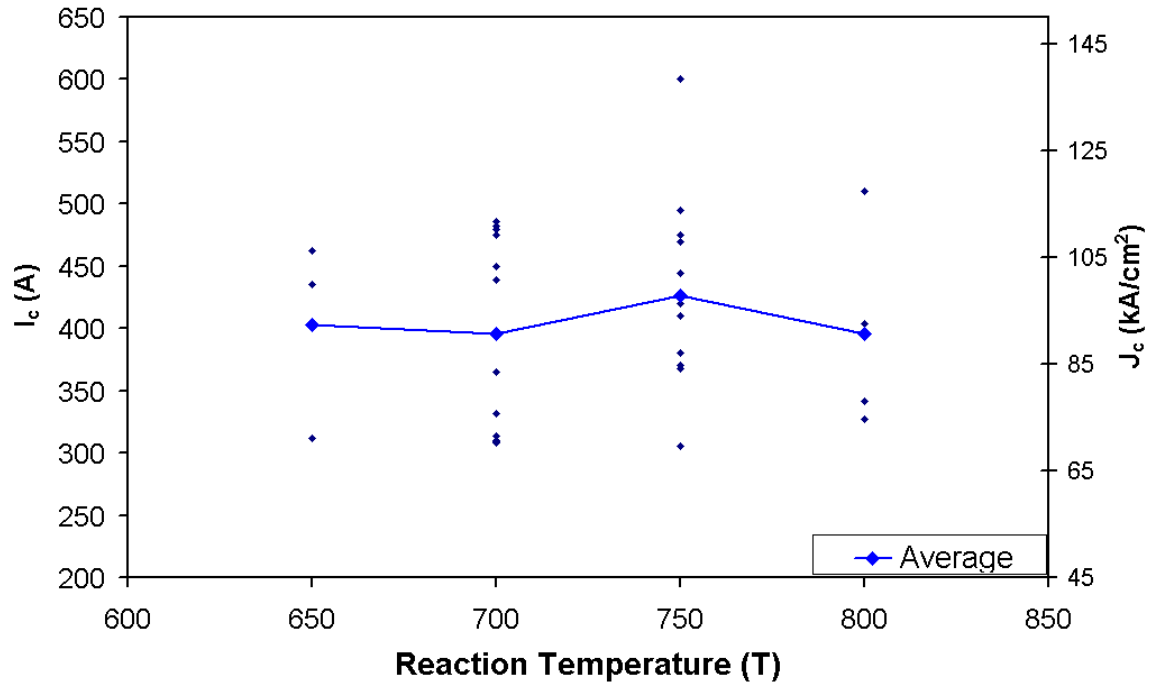


FIGURE 5.7 Variation of I_c (4.2 K) values for 10 at% doped wires

5.2 Conclusions

Wire drawing using a conventional drawing bench is an effective means of developing long lengths of dense, steel sheathed, MgB_2 wires. Long length wires with an outer diameter of 1.215 mm and a superconducting core diameter of 0.75 mm were fabricated.

The bright particles seen in figure 5.3 cannot be easily distinguished by their contrast, but their differences in morphology give clues to their composition. Particles were either long and thin (*a*) or round and bulky (*b*). It is known that Mg melts at 650 °C. If particle *a* has high concentrations of Mg, its long and thin shape may be due to melting. This hypothesis is supported by EDS analysis. Figure 5.4 shows that particle *a* has a much

higher concentration of Mg than particle *b*. On the contrary, V has a high melting point (~1900 °C) and is not expected to melt at the reaction temperatures used. Therefore it is possible to speculate that particle *b* is primarily composed of V, which is supported by its EDS spectrum.

The presence of unreacted Mg in the samples, as seen from the Mg rich particles in the electron micrographs, suggests that the material is not Mg deficient. Samples of $\text{Mg}_{1-x}\text{V}_x\text{B}_2$ compositions would be Mg deficient if V is not entering the superconducting phase. The absence of any indication of Mg deficiency in V doped compositions suggests that V might be replacing Mg in the MgB_2 matrix. This is supported by EDS analysis of the main MgB_2 phase in figure 5.4 where a small V peak was found. It is important to note that despite the term “spot analysis” the characteristic x-rays in an EDS scan come from a volume of interaction between the material and the incident electron beam, which is approximately $5\text{ }\mu\text{m}^3$ for MgB_2 . So it is possible that the V peak is coming from either finely dispersed particles, small enough to avoid detection at high magnifications (5000 X), or a particle beneath the surface. The latter is unlikely because similar EDS scans were obtained in the analysis of the MgB_2 phase. V replacing Mg is only a possible explanation to why doped samples are not Mg deficient; it is still unclear why Mg precipitates are forming. In addition, EDS analysis of particle *b* suggests that the round, bulky particles are V rich. The presence of V rich particles does not rule out the possibility that a portion of V is entering the MgB_2 phase.

The rather large scatter in the results of I_c measurements (standard deviation = ~ 92 A) made it difficult to see if there are any systematic enhancements in I_c of V doped samples. The spread in I_c data might be due to the inhomogeneity of the superconducting core. The microstructure of every sample measured was not examined. So it is possible that the distribution of second phase precipitates might have changed along the length of the wire (avg. tap length = 20 mm). Although these precipitates act as pinning sites, which improve in-field J_c properties, they are too large to be considered “effective”. An ideal pinning site is large enough to contain one fluxon, which is on the order of the coherence length (nms), but small enough to not waste overall superconductor volume, which would reduce J_c . If precipitates were to group together, they could limit the amount of current flowing through the conductor, which would result in a lower I_c measurement. To ensure proper mixing, researchers often subject a material to multiple mixing and heating cycles. This is not possible with our samples for two reasons; first, because Mg is volatile, and each heating would lead to the loss of more Mg and secondly, mixing of the samples becomes impossible once they were in wire form.

Another possible reason for variation in I_c measurements might be the use of a steel sheath. Although steel is a low cost sheath material, its resistivity lowers stability and makes I_c measurements difficult. To understand how steel is affecting the reproducibility of measurements, it may be necessary to remove the steel sheath and conduct magnetization measurements on the superconducting core.

Ignoring the reproducibility problems, there seems to be little change in I_c values with increasing dopant concentration. This is significant because we are substituting up to 15 at% of Mg for V. If we were to argue that V was not entering the MgB_2 matrix then this loss in Mg would leave an excess of unreacted B. Figure 5.8 shows how a small substitution could lead to approximately 22% of non-superconducting material within the 15 at% sample. To make this conclusion, it is assumed that powders are mixed well, homogeneously distributed throughout the wire, and that all of the Mg is being used in the MgB_2 reaction. Our microstructure investigation indicates that there is Mg rich particles still present in reacted wires. So the percentage of non-superconducting material might be higher. Assuming a constant density among constituents, this suggests that 15 at% samples have a 22 % smaller superconducting cross-section than undoped (0 at%) samples. If V were not entering the MgB_2 matrix, one would expect to see a reduction in I_c measurements with increasing V substitution. Figure 5.6 shows that doped samples are capable of reaching high I_c values; in fact, the highest current measured was a 15 at% sample. The fact that I_c values are not reduced with V substitution suggests that either V is successfully substituting for Mg or the addition of V is somehow counteracting the loss of Mg. This could be accomplished by increasing connectivity or density, or possibly by some other mechanism not yet understood.

For a 15 at% doped wire:

$$\begin{aligned}
 0.85 \text{ Mg} + 0.15 \text{ V} + 2 \text{ B} &= (\text{Mg}_{0.85}\text{B}_{1.7}) + 0.15 \text{ V} + 0.3 \text{ B} \\
 50 \text{ amu of (Mg-V-B)} &= 39 \text{ amu of (MgB}_2\text{)} + 11 \text{ amu of (V + B)} \\
 &= 78\% (\text{MgB}_2) + 22\% (\text{V + B})
 \end{aligned}$$

Figure 5.8 Percentage of non-superconducting material present in 15 at% V doped wires if V is not entering the MgB_2 phase

CHAPTER 6

SUMMARY AND SUGGESTIONS FOR FUTURE WORK

The effects of V doping on microstructural and superconducting properties of MgB_2 bulk and wires have been investigated. Samples having the nominal composition $\text{Mg}_{1-x}\text{V}_x\text{B}_2$ ($x = 0, 0.05, 0.10, 0.15$) have been fabricated. Characterization of superconducting samples was carried out using XRD, SQUID, ESEM/EDS, and I_c measurements. Results show an enhancement of superconducting properties with V doping. Wires with J_c values as high as $1.4 \times 10^5 \text{ A/cm}^2$ have been achieved.

XRD analysis was conducted on bulk samples of all V dopant compositions reacted at 800°C . Samples with a peak reaction time of 0.3 hour showed an increase in MgB_4 as V concentration was increased, while samples reacted for 1.0 hour did not. While impurity formation appears to be increasing with shorter reaction times, magnetization studies have shown an increase in hysteresis loop widths (ΔM) with shorter reaction time. It is suggested that shorter peak reaction times may limit grain growth, which in turn will increase grain boundary density. Grain boundaries have been shown to act as pinning centers in MgB_2 [21]. Due to the large variation in I_c values, it was difficult to optimize the heat treatment for Mg-V-B wires. It was found that the 700°C for 0.5 hour heat treatment produced the samples with the highest I_c values for the 0, 5, and 15 at% samples. The maximum I_c for 10 at% was attained by heat-treating samples for 750°C for 0.5 hour.

It was found that Ni is not an appropriate sheath material for samples heat treated at elevated temperatures for an extended amount of time. The reaction between Ni and the superconducting core will undoubtedly lead to reduction in superconducting and mechanical properties. On the other hand, low carbon (1010 or 1020) steel did not show any sign of a reaction between the core and sheath. Although steel is chemically compatible, wires with a diameter less than 1.215 mm could not be fabricated due to the level of work hardening. An intermediate stress relief anneal is necessary to attain smaller wire diameters.

XRD investigation as well as ESEM and EDX analysis indicates that bulk samples reacted for 1 hour and wire samples reacted for 0.5 hour are not Mg deficient. An explanation for the lack of Mg deficiency could be that V is entering the MgB_2 phase. TEM analysis is needed to confirm this. Magnetization measurements of bulk samples

and I_c measurements of groove rolled wires show an increase in performance with increasing dopant percentage, up to 10 at%. Due to the scatter in I_c values, it is difficult to see improvements in V doped drawn wires. While the optimum dopant percentage is not clear, it is important to note that no dopant percentage is spoiling the properties. If V were not entering the MgB_2 matrix, the lack of Mg would leave unreacted B. In 15 at% wires, at least 22 % of the mass would be non-superconducting. If this were true, a drop in I_c should have occurred.

The results described have shown that V doping has the potential to improve MgB_2 's performance. Further studies are needed to understand the mechanism by which V is affecting the microstructure and properties of MgB_2 wires. Detailed measurements of I_c in background magnetic fields, magnetization measurements, and TEM analysis of the microstructure are needed.

REFERENCES

1. H. Kamerlingh Onnes, *Leiden Commun.*, 120b, 112b, 124c (1911).
2. Bednorz, G. and Muller, K.A. *Z. Phys. B* **64**, 189-193 (1986)
3. M.K. Wu, J.R. Ashburn, C.J. Torng, P.H. Hor, R.L. Meng, L. Gao, Z.J. Huang, Y.Q. Wang, and C.W. Chu, *Phys. Rev. Lett.* **58**, 908-912 (1987)
4. H. Maeda, Y. Tanaka, M. Fukutomi, and T. Asano, *Jpn. J. Appl. Phys. Lett.* **27**, L209 (1988)
5. A. Goyal, D.P. Norton, J.D. Budai, M. Paranthaman, E.D. Specht, D.M. Kroeger, D.K. Christen, Q. He, B. Saffian, F.A. List, D.F. Lee, P.M. Martin, C.E. Klabunde, E. Hatfield, V.K. Sikka, *Appl. Phys. Lett.* **69** (1996) 1795.
6. D. Shi, “*High Temperature Superconducting Materials Science and Engineering: New Concepts and Technology*”, 1st ed., Elsevier Science & Technology Books (1995)
7. D. Larbalestier, A. Gurevich, D. M. Feldmann, A. Polyanskii, *Nature*, **414**, 368 (2001).
8. Dew-Hughes, D. *Phil. Mag.* **55**, 449-459 (1987)
9. J. Nagamatsu, N. Nakagawa, T. Muranka, Y. Zenitani and J. Akimitsu *Nature* **410** 63 (2001).
10. S.L. Bud’ko, C. Petrovic, G. Lapertot, C.E. Cunningham, P.C. Canfield, M-H Jung, A.H. Lacerda, *Phys. Rev. B* **63**, 220503 (2001).
11. S.L. Bud’ko, G. Lapertot, C. Petrovic, C.E. Cunningham, N. Anderson, P.C. Canfield, *Phys. Rev. Lett.* **86**, 1877 (2001).
12. S. Lee, H. Mori, T. Masui, Y. Eltsev, A. Yamamoto, S. Tajima “*Growth, structure analysis and anisotropic superconducting properties of MgB₂ single crystals*”, cond-mat/0105545
13. N. Klein, B.B. Jin, J. Schubert, M. Schuster, H.R. Yi, A. Pimenov, A. Loidl, S.I. Krasnosvobodtsev “*Energy gap and London penetration depth of MgB₂ films determined by microwave resonator measurement*”, cond-mat/0107259
14. R. Jin, M. Paranthaman, H.Y. Zhai, H.M. Christen, D.K. Christen, D. Mandrus, “*Unusual Hall effect in superconducting MgB₂ films: Analogy to High-T_c Cuprates*”, cond-mat/0104411
15. D. Kaczorowski, A.J. Zaleski, O.J. Zogal, J. Klamut, “*Incipient superconductivity in TaB₂*” cond-mat/0103571
16. D. P. Young, P. W. Adams, J. Y. Chan, F. R. Fronczek, “*Structure and Superconducting Properties of BeB₂*” condmat/ 0104063
17. M. Dhallé, P. Toulemonde, C. Beneduce, N. Musolino, M. Decroux and R. Flükiger *Physica C* **363** 155 (2001).
18. C. Buzea, T. Yamashita, *Supercond. Sci. Technol.* **14**, R115 (2001)
19. W. Goldacker, S.I. Schlachter, S. Zimmer, H. Reiner, *Supercond. Sci. Technol.* **14**, 787-793 (2001)
20. C.B. Eom, M.K. Lee, J.H. Choi, L. Belenky, X. Song, L.D. Cooley, M.T. Naus, S. Patnaik, J. Jiang, M. Rikel, A. Polyanskii, A. Gurevich, X.Y. Cai, S.D. Bu, S.E. Babcock, E.E. Hellstrom, D.C. Labalestier, N. Rogado, K.A. Regan, M.A. Hayward, T. He, J.S. Slusky, K. Inumaru, M.K. Haas, R.J. Cava, *Nature*, **411**, 558 (2001)

21. D.C. Larbalestier, L.D. Cooley, M.O. Rikel, A.A. Polyanskii, J. Jiang, S. Patnaik, X.Y. Cai, D.M. Feldmann, A. Gurevich, A.A. Squitieri, M.T. Naus, C.B. Eom, E.E. Hellstrom, R.J. Cava, K.A. Regan, N. Rogado, M.A. Hayward, T. He, J.S. Slusky, P. Khalifah, K. Inumaru and M. Haas *Nature* **410** 186 (2001).
22. Y. Bugoslavsky, L.F. Cohen, G.K. Perkins, M. Polichetti, T.J. Tate, R. Gwilliam and A.D. Caplin *Nature* **411**, 561-563 (2001)
23. Yanwei Ma, H. Jumakura, A. Matsumoto, K. Togano, *App. Phys. Lett.* **83**, 1181 (2003)
24. S.X. Dou, J. Horvat, S. Soltanian, X.L. Wang, M.J. Qin, S.H. Zhou, H.K. Liu, P.G. Munroe, "Transport critical current density in Fe-sheathed nano-SiC doped MgB₂ wires". Presented at ASC 2002, Houston, cond-mat/0208215.
25. J.S. Slusky, N. Rogado, K.A. Regan, M.A. Hayward, P. Khalifah, T. He, K. Inumaru, S.M. Loureiro, M.K. Haas, H.W. Zandbergen, R.J. Cava, *Nature* **410**, 343 (2001)
26. K. Tachikawa, Y. Yamada, O. Suzuki, M. Enomoto, M. Aodai, *Physica C*, **382**, 108-112 (2002)
27. Y. Zhao, Y. Feng, C.H. Cheng, L. Zhou, Y. Wu, T. Machi, Y. Fudamoto, N. Koshizuka, and M. Murakami, *Appl. Phys. Lett.* **79** 1154 (2001).
28. Y. Zhao, D.X. Huang, Y. Feng, C. H. Cheng, T. Machi, N. Koshizuka, and M. Murakami, *Appl. Phys. Lett.* **80** 1640 (2002).
29. U.P. Trociewitz, P.V.P.S.S. Sastry, A. Wyda, K. Crockett, and J. Schwartz, *IEEE Trans. Appl. Supercond.* **11** 3320 (2003).
30. J.C. Slater, *J. Chem. Phys.* **39**, 3199 (1964)
31. "Fundamentals of Welding" in *Welding Handbook*, **Vol 1**, 7th ed., American Welding Society, (1976)
32. W.D. Callister, Jr., "Materials Science and Engineering: An Introduction", 5th ed., John Wiley & Sons, Inc. (2000)
33. C.P. Bean, *Rev. Mod. Phys.* **36** (1964) 31
34. A.C. Rose-Innes, E.H. Rhoderick, International Series on solid State Physics, Vol. 6, "Introduction to Superconductivity, Second Edition", Pergamon Press, New York (1988)
35. M. Kambara, N.H. Babu, E.S. Sadki, J.R. Cooper, H. Minami, D.A. Cardwell, A.M. Campbell and I.H. Inoue *Supercond. Sci. Technol.* **14** L5 (2001).
36. Y. Takano, H. Takeya, H. Fujii, H. Kumakura, T. Hatano and K. Togano *Appl. Phys. Lett.* **78** 2914 (2001).
37. M. Eisterer, M. Zehetmayer, S Tönies, H.W. Weber, M. Kambara, N. Hari Babu, D.A. Cardwell and L.R. Greenwood, *Supercond. Sci. Technol.* **15** L9 (2002).
38. J. Wang, Y. Bugoslavsky, A. Berenov, L. Cowey, A.D. Caplin, L.F. Cohen, J.L. MacManus Driscoll, L.D. Cooley, X. Song and D.C. Larbalestier, *Appl. Phys. Lett.* **81** 2026 (2002).
39. S.X. Dou, S. Soltanian, J. Horvat, X.L. Wang, S.H. Zhou, M. Ionescu, H.K. Liu, P. Munroe and M. Tomsic *Appl. Phys. Lett.* **81** 3419 (2002).

BIOGRAPHICAL SKETCH

Oscar E. Castillo was born May 27, 1979 in Lima, Peru. Soon after his birth he, his parents, and his two older sisters moved to the United States. After a few years in Indiana his family settled in Tallahassee, FL where he spent the majority of his childhood.

In 1997 he was accepted into the Mechanical Engineering department at Florida State University. After graduating in 2002, Oscar decided to continue his education at Florida State and pursue a Master's degree. As a graduate student he worked with Dr. Justin Schwartz as a research assistant at the Center for Advanced Power Systems. Oscar's research focused on the study of MgB_2 and the possible effects of Vanadium on microstructural and superconducting properties.